Old Dominion University
ODU Digital Commons

Electrical & Computer Engineering Theses & Dissertations
Electrical & Computer Engineering

Spring 1991

Monte Carlo Simulation of Millimeter-Wave Gunn Effect Oscillators

Ramani Vaidyanathan
Old Dominion University

Follow this and additional works at: https://digitalcommons.odu.edu/ece_etds

Part of the Computational Engineering Commons, Electrical and Electronics Commons, Electronic Devices and Semiconductor Manufacturing Commons, and the Semiconductor and Optical Materials Commons

Recommended Citation

Vaidyanathan, Ramani. "Monte Carlo Simulation of Millimeter-Wave Gunn Effect Oscillators" (1991). Master of Science (MS), Thesis, Electrical & Computer Engineering, Old Dominion University, DOI: 10.25777/e3v9-fv62
https://digitalcommons.odu.edu/ece_etds/549

This Thesis is brought to you for free and open access by the Electrical & Computer Engineering at ODU Digital Commons. It has been accepted for inclusion in Electrical & Computer Engineering Theses & Dissertations by an authorized administrator of ODU Digital Commons. For more information, please contact digitalcommons@odu.edu.

Monte Carlo Simulation of Millimeter-Wave Gunn Effect Oscillators

by

Ramani Vaidyanathan
B.E. in Electrical and Electronics Engineering
Bharathidasan University, Trichy, INDIA

A Thesis Submitted to the Faculty of
Old Dominion University in Partial Fulfillment of the
Requirements for the Degree of

MASTER OF SCIENCE

ELECTRICAL ENGINEERING

with an Emphasis on Physical Electronics

OLD DOMINION UNIVERSITY
May 1991

Approved by:

Ravindra P. Joshi (Director)

Hasan H. Erkaya

Sacharia Albin

ABSTRACT

Monte Carlo simulations have been carried out to investigate the performance of microwave Gunn oscillators. Three separate aspects of the simulation problem have been comprehensively addressed in this work. First, the presence of an external circuit has been self-consistently incorporated into the calculations. The inclusion of the external circuit facilitates a study of the circuit controlled regime, and correctly models effects arising from the time dependent boundary conditions. Secondly, microscopic details of the electronic relaxation mechanisms which ultimately control the frequency response limits, have been taken into account through an iterative Monte Carlo-Poisson scheme. This procedure overcomes a potential shortcoming of many previous analytical simulations which have relied on the steady state velocity-field characteristics for obtaining the microwave response. Comparisons between conventional GaAs Gunn diodes including a doping notch in the active layer have been made with $Al_xGa_{1-x}As$ heterojunction cathode structures. Particular attention has been focussed on the heterojunction cathode effects. Impact on the changes in the operating characteristics, the ac conversion efficiency, and the power output arising from variations in the doping profile and alloy composition have been studied. Finally, results from some pertinent comparisons between conventional bulk oscillators and hetero-structure devices have also been obtained. We conclude that heterostructure Gunn diodes show improvements in performance over conventional Gunn devices at high voltages. In addition, appropriate tailoring of the doping profile can enhance the ac conversion efficiency.

ACKNOWLEDGEMENTS

I would like to express my sincere appreciation and gratitude to my advisor, Dr. Ravindra P. Joshi for his guidance, encouragement, and continual support during the course of my graduate studies at Old Dominion University. His help, patience, and friendship have made my education a truly enjoyable experience. I also wish to express my special thanks to Dr. Hasan Erkaya and Dr. Sacharia Albin for their comments on this research work and for being on my committee. I also convey my sincere thanks to Dr. Vishnukumar Lakdawala for his help and guidance throughout my graduate studies.

I must acknowledge the valuable help and assistance of Mike Kennedy for providing the graphics routine used to obtain the graphs in this work. My thanks also go to Lucy Thomas and Mandakini Kale for their moral support which helped me maintain my sanity.

Most of all, I could never have completed my education without the support of my family, especially my father.

TABLE OF CONTENTS

Page

List of Tables v

List of Figures vi

Chapter

1. Introduction 1

    Conventional Gunn Diode Oscillators 3

    Enhanced Gunn Diode Design 4

    Scope of Research 6

2. Physical Characteristics of Gunn Devices 8

    Microwave Semiconductor Junction Devices 9

    Local Negative Conductivity in Gallium Arsenide 12

    Development of Criteria for Transfer 15

    The Operating Modes of Gunn Devices 19

    Space-charge Growth Mechanism 20

    Modes of Operation 25

    Schemes for Improving Device Performance 27

3. Numerical Simulation Scheme for the Gunn Diode 30

    Monte Carlo Simulation 31

The Solution of Poisson's Equation 37
Velocity-field Curve 44
4. Gunn Diode as a Relaxation Oscillator 52
The Device Model 53
Numerical Simulations 55
Discussion of Results 60
5. Summary and Conclusions 86
Concluding Summary 86
Suggestions for Future Work 87
References 90

LIST OF TABLES

Table | Page

I. Properties of GaAs at 300 K 38

II. Material parameters of GaAs Monte Carlo program 39

III. RF performance of Gunn oscillators 84

LIST OF FIGURES

Figure		Page
1	Current-voltage characteristics of a typical Tunnel diode	10
2	Conduction-band structure of GaAs	14
3	Curves of velocity against electric field for carriers in GaAs	18
4	Formation of electron accumulation layer in a perturbed medium of negative resistivity	22
5	Formation of electron dipole layer in a perturbed medium of negative resistivity	24
6	Time dependent variation of internal electric field across the Gunn device	26
7	Flow-chart of the Ensemble Monte Carlo program	33
8	Flow-chart of scattering selection in Monte Carlo simulations	36
9	Flow-chart of a device Ensemble Monte Carlo program	40
10	The doping profile of the simulated device structure for GaAs notch oscillator	43
11	Electronic distribution profile across the Gunn device under zero bias conditions	45
12	Electric field distribution profile across the Gunn device under zero bias conditions	46

13 Voltage distribution profile across the Gunn device under zero bias conditions 47

14 Transient electron velocity curves for different values of electric field 50

15 Turn-off transient electron velocity curve for the electric field of 20 kV/cm within an inhomogeneous structure 51

16 Schematic diagram of the parallel resonant circuit used for the simulation of a Gunn diode oscillator 56

17 The simulated device structure for $Al_{0.3}Ga_{0.7}As$-GaAs-GaAs heterostructure oscillator 59

18 Valley occupation showing electronic distribution in the Γ, and L valleys for the heterostructure oscillator a) at the time instant T/4, and b) at the time instant T/2, for a bias voltage of V_B=2.0 volts 61

19 Valley occupation showing electronic distribution in the Γ, and L valleys for the heterostructure oscillator a) at the time instant 3T/4, and b) at the time instant T for a bias voltage of V_B=2.0 volts 62

20 Comparison of electron population in Γ, and L valleys at the time instant 3T/4 at a bias of V_B=2.0 volts for the devices a) notch oscillator, and b) heterostructure oscillator 63

21 Diode voltage waveform of a notch-type Gunn oscillator at a bias of 3.0 volts 65

22 Total circuit current waveform of a notch-type Gunn oscillator at a bias of 3.0 volts 66

23 Diode current waveform of a notch-type Gunn oscillator at a bias of 3.0 volts 67

24 Diode voltage waveform of a heterostructure oscillator with an aluminium composition coefficient of 0.30 at a bias of 2.0 volts . . 68

25 Total circuit current waveform of a heterostructure oscillator with an aluminium composition coefficient of 0.30 at a bias of 2.0 volts 69

26 Diode current waveform of a heterostructure oscillator with an aluminium composition coefficient of 0.30 at a bias of 2.0 volts . . 70

27 Diode voltage waveform of a heterostructure oscillator with an aluminium composition coefficient of 0.30 at a bias of 3.0 volts . . 71

28 Total circuit current waveform of a heterostructure oscillator with an aluminium composition coefficient of 0.30 at a bias of 3.0 volts 72

29 Diode current waveform of a heterostructure oscillator with an aluminium composition coefficient of 0.30 at a bias of 3.0 volts . . 73

30 Snapshot picture of the spatial electronic distribution within the Heterostructure Gunn diode at a bias of 3.0 volts at the time instant T/4 (one-quarter cycle) 77

31 Snapshot picture of the spatial electronic distribution within the Heterostructure Gunn diode at a bias of 3.0 volts at the time instant T/2 (one-half cycle) 77

32 Snapshot picture of the spatial electronic distribution within the Heterostructure Gunn diode at a bias of 3.0 volts at the time instant 3T/4 (three-quarter cycle) 77

33 Snapshot picture of the spatial electronic distribution within the Heterostructure Gunn diode at a bias of 3.0 volts at the time instant T (one full cycle) 78

34 Simulated structure of Heterostructure oscillator with a graded injector at the cathode 80

35 Simulated structure of Heterostructure oscillator with a graded doping in logarithmic fashion in the active region 82

CHAPTER 1

INTRODUCTION

In recent years, applications of heterojunctions, formed by the joining of two dissimilar semiconductors to enhance device performance, have been the subject of intensive research by electronics companies throughout the world. The advent of some of the latest and most sophisticated semiconductor growth techniques now allow the fabrication of multiple heterojunctions separated by literally a few atomic layers. By a judicious choice of the two semiconductors and the growth conditions it is possible to produce single crystal multilayers in which the semiconductor bandstructure is tailored in the growth direction. Indeed, two classes of devices relying on the physics of heterojunctions have already reached the marketplace. These are the quantum well laser (QWL) [1] and the high electron mobility transistors (HEMT) [2].

There are, of course, many other possible applications for such band-gap engineering. We have chosen to study the use of heterojunction technology as a solid-state microwave source - the transferred electron oscillator (TEO) or Gunn diode [3]. Starting from the initial discovery of the negative differential resistance [4], the phenomena of semiconductor based microwave signal generation, amplification and processing has run the course of truly exciting research endeavor. Various theoretical aspects have been studied in order to understand the physical phenomena, characterize the different device operating modes, probe fundamental device limitations, and to analyze performance

parameters such as noise spectra and microwave power conversion efficiencies. Despite the abundant literature available on the subject, a reevaluation of Gunn-effect electronics probably becomes necessary for several reasons. First our understanding of the subtleties of electron dynamics has improved significantly over the last decade. Better values for the material parameters, intervalley separation thresholds [5], phonon-eigen energies [6], and electron-phonon coupling constants [7] have been obtained through experimentation. Hence, a Monte Carlo analysis of Gunn oscillator performance becomes very fruitful from the standpoint of improved accuracy and realistic predictions.

Another reason for carrying out Monte Carlo simulations arises from recent technological developments in the area of semiconductor heterostructures. Advances in semiconductors growth techniques such as Molecular Beam Epitaxy (MBE) and Metal Organic Chemical Vapor Deposition (MOCVD) techniques have now made it possible to engineer novel heterojunction devices with precise control over both material composition and the geometric dimensions [8]. The most significant property of such heterojunctions which makes them particularly useful for microwave applications, is their ability to impart large energy increments over very short distances leading to hot carrier injection. The sudden (kinetic) energy increases are made possible during the traversal of the heterojunction, as the carriers move from the higher bandgap side into the low bandgap material. Typical length scales associated with the transition process are of the order of a few Angstroms, and hence well below the characteristic scattering distances.

1.1 Coventional Gunn Diode Oscillators

Currently, Gunn effect oscillators based on the electronic k-space transfer process are among the most promising candidates for semiconductor microwave applications. A conventional GaAs Gunn diode consists of three layers; containing a relatively low doped transit region ($\sim 10^{16}$ cm^{-3}) sandwiched between two very highly doped contact layers, forming an n^+-n^--n^+ structure. A bias is applied across the contact layers causing electrons to flow from the cathode to the anode. As the electrons are accelerated in the electric field they gain energy and momentum. During this acceleration they also lose energy because of the inelastic scattering mechanisms described later in chapter 3. The profile of potential in the transit region under bias is non-linear, with its gradient, the electric field, ever increasing as it approaches the anode. As the electric field becomes larger, the rate of gain of energy from the electric field exceeds the rate of loss from inelastic scattering, and the electron has, on average, a net gain of energy with time and distance travelled. If the transit region and the applied bias are sufficiently large, then at some point, the electrons gain enough energy to transfer from the central Γ valley to an upper satellite (L or X) valley. This is explained in detail in section 2.3. The spatial region extending from the cathode up to this point is known as the dead zone. The rate of loss of energy in the dead-zone because of phonon emission and other inelastic scatterings can be large, and this contributes to the poor efficiency found in this type of device. In addition, since significant intervalley transfer does not take place in this region, negative differential mobilities which contribute to the active power are also absent. Hence, the dead zone needs to be reduced through suitable design.

1.2 Enhanced Gunn Diode Design

The above concept is relatively easy to understand in qualitative terms. The difficulties start to arise when one thinks about the systems applications for this sort of device as an oscillator. There are several performance specifications which need to be optimized simultaneously. The two primary specifications for an oscillator are the frequency at which it operates and the power it can deliver. The limit to the power output is the amount of charge that can collect in the accumulation layer without the electric field at the anode exceeding the breakdown electric field of GaAs. The oscillating frequency, as stated above, is related to the transit time of the accumulation layer from the point of formation to the anode.

To maximize the power and efficiency for a particular length, the accumulation layer should form as close to the cathode as possible. Thus by choosing an appropriate transit region length and doping, it is possible to maximize the power (at some bias) for a desired frequency. The solution is to design a Gunn diode where the critical field point is fixed at the cathode. The structure should have the accumulation layer start as near the cathode as possible to sustain the accumulation formation and propagation, which is responsible for microwave oscillations.

In view of the above discussion, it becomes apparent that the problem of attaining optimized device design is non-trivial. General guidelines and probable trends towards optimization can, however, be successfully obtained by simulating a variety of device structures with different doping profiles and material composition. The current goal is to take a step in this direction by focussing on both the conventional and the heterostructure

Gunn oscillator devices. Since the conventional structures have already been investigated in the past, the current emphasis will be on heterostructure oscillators. By simulating various device parameters, a comparative performance study as a function of the device structure, doping variations, operating voltages and compositional grading profiles will be comprehensively included. For our simulation purposes, we shall include both the conventional notch oscillator and a heterojunction configuration as shown later in Figures 10 and 17 respectively. The notch structure will be included in the analysis because it serves as a standard accuracy check of the Ensemble Monte Carlo (EMC) simulations to be used, and allows relative comparisons to be made with heterostructure oscillators.

Many simulations of Gunn effect oscillators in the past, have relied on a variety of simplifying assumptions. For example, early studies by Copeland [9] assumed that electrons could respond instantaneously to changes in the electric fields. In subsequent work [10, 11], the electronic relaxation effects were explicitly included, but the analysis nonetheless used approximations to the actual carrier distribution functions. Lebwohl and Price using the Monte Carlo method [12] were the first to study Gunn effect devices without making any approximations for the electronic distribution functions. Unfortunately, however their analysis did not include the correct bandgap ordering, since the Γ^c_6-L^c_6-X^c_6 sequence was experimentally established at a later stage [13]. In a more recent work, many of the previous problems were addressed by Tully [14]. His simulations, however, were restricted to the study of homojunction devices. Here,we shall attempt to examine both the conventional notch oscillators and heterojunction devices, while making suitable comparisons.

Before summarizing the scope of this project, a brief discussion outlining the advantages of heterostructure oscillators is perhaps in order. First, by eliminating the notch structure, it becomes possible to reduce the physical dimensions and increase the corresponding device transit frequency. An added advantage accrues from the enhanced flexibility in tailoring device performance through material grading and compositional changes. Hence, the use of a suitable graded $Al_xGa_{1-x}As$ injector should improve its oscillatory performance. However, the doping profile near the cathode must be controlled so that the field from the ionized impurities in the depletion layer set up, when the $Al_xGa_{1-x}As$ injector is forward biased, does not suppress the formation of charge instabilities. In order to confirm these design criteria we shall perform self-consistent Monte Carlo simulations which are explained in the following chapters.

1.3 Scope of Research

The present work is dedicated to the study of the Gunn devices for microwave oscillations using the Ensemble Monte Carlo Technique. In chapter 2, a brief review of the physical characteristics of microwave devices is presented. In particular, the objective of this chapter is to show that time varying, spatially dependent internal charge distributions within the device are necessary ingredients for microwave oscillations. Also, it explains the role of material parameters, the device geometries and external circuit elements in controlling output microwave frequencies.

In chapter 3, the principles of Monte Carlo method, applied to the study of semiconductors, are introduced. The general features of EMC algorithm used for the self

consistent simulation of semiconductor devices are thoroughly discussed. This chapter also explains the implementation of the algorithms for the solution of Poisson's equation.

The EMC model implemented for the simulation of the Gunn diode is presented in chapter 4. The complete details concerning the modeling of the Gunn diode and its interaction with the external circuit are discussed, followed by the presentation and the analysis of the results obtained from the simulations.

Chapter 5 contains a summary of the conclusions obtained for a large signal simulation of a millimeter-wave Gunn effect oscillator. Also, recommendations for future research which could produce improvements in the performance of Gunn devices are outlined.

CHAPTER 2

PHYSICAL CHARACTERISTICS OF GUNN DEVICES

The first chapter described the overall research objectives and included details of the work to be performed. In this chapter, several important aspects relating to microwave Gunn oscillators will be discussed. To begin with, a brief comparison between various semiconductor microwave devices will be presented to highlight the relative advantages in using Gunn diodes. This will be followed by a short outline of the relevant device physics in section 2.3. In particular, the intervalley electron transfer mechanism responsible for the negative differential resistance phenomena will be discussed. Next, some of the common modes of device operation will be examined in section 2.4. The objective will be to show that time-varying, spatially dependent internal charge distributions within the device are necessary ingredients for microwave oscillations. The role of material parameters, the device geometries, and external circuit elements in controlling the output microwave frequencies will also be discussed in section 2.4. Finally, section 2.5. will present some schemes for improving device performance based on suitable changes in the semiconductor materials and through the use of alternative heterojunction structures.

2.1 Microwave Semiconductor Junction Devices

Research in semiconductor based microwave technology for generation, amplification, and signal processing applications has led to the fabrication of a large variety of solid state devices in bulk semiconductors. Included among these are Tunnel diodes, Varactor diodes, IMPATT and BARITT devices and Gunn-effect oscillators. Tunnel diodes exhibit a negative differential conductance region (NDR) in their current-voltage characteristic as shown in Figure 1. They are capable of operating up to frequencies in excess of 100 GHz, because of the inherently high speed tunneling of electrons through the potential barrier of a p-n junction. However, since the tunnel effect and hence the range of negative conductance, is restricted to voltages less than the band-gap of the semiconducting material ($\approx$ 1 V), the attainable r.f. power levels are disappointingly low. In addition, both the power dissipating capability and the ruggedness of the tunnel device usually suffers if sizes are reduced to lower the parasitics. In Varactors, the junction depletion capacitance is made to change through variations in the applied reverse bias. There are, however, two additional difficulties associated with such a structure. First, since destructive avalanche multiplication can occur with very high reverse bias, a natural limit for the useful operating range of the diode is automatically set. Secondly, it is not an active oscillator and requires the presence of passive circuit elements.

In another family of devices, represented by the IMPATT, TRAPATT, and BARITT diodes, the desired NDR is achieved by controlling the phase shifts between the device current and applied voltage by a two-step process. The first involves an avalanche

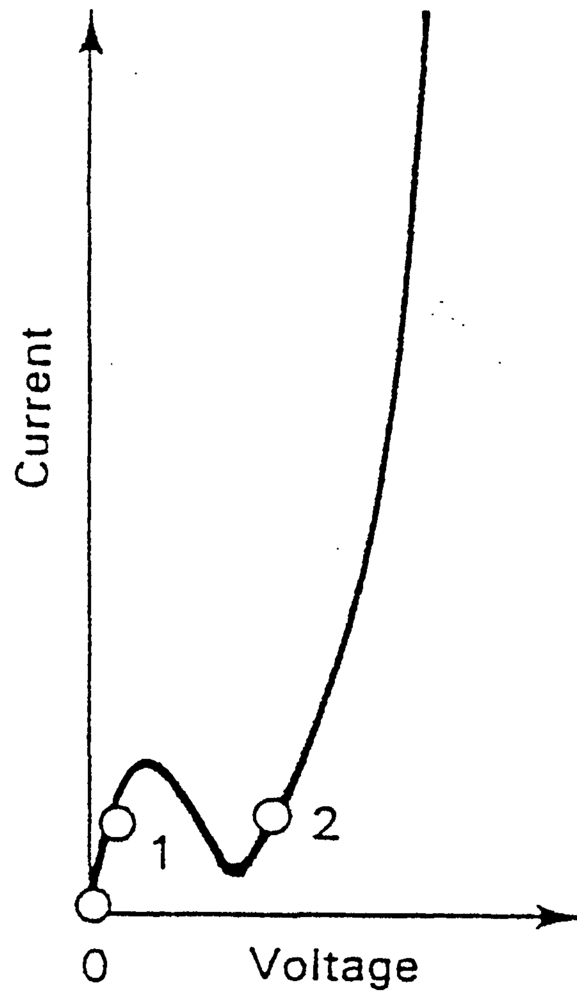

Figure 1. Current-voltage characteristics of a typical Tunnel diode

breakdown inside a reverse biased p-n junction controlled by an applied r.f. field. This process introduces a 90° phase lag in the current waveform. The subsequent carrier drift along the device contributes to an additional phase delay giving rise to the negative power dissipation mechanism. There are, however, two noteworthy difficulties with the transit-time devices for circuit applications: (1) the noise is high, and sensitive to operating conditions; and (2) the large electronic reactances present are strongly dependent on oscillation amplitudes, and require unusual care in circuit design to avoid detuning or even burnout of the diode. In addition, thermal and shot noise associated with the p-n junction and the avalanche process, are responsible for the performance degradation.

Because of the above disadvantages, consideration was given to the possibility of producing bulk negative conductance in a homogeneous semiconductor (i.e. without p-n junctions) for the generation and amplification of r.f. signals. It seemed likely that by abandoning p-n junctions, with their restricted active volume and their associated capacitances, it might be possible to achieve higher r.f.powers and frequencies, reduce noise levels with the added advantage of simpler manufacture. Such a microwave oscillator based on a bulk semiconductor effect was made possible with the discovery of the Gunn effect.

The Gunn diode operation is based on the transferred electron effect which arises from the bulk properties of semiconductors and does not depend, on either the junction or contact properties. In addition, the effect is independent of total voltage or current, and is not affected by magnetic fields or different types of contacts [15]. Furthermore, it occurs in n-type materials only, since it results from transitions within the electronic

band-structure. The occurrence of such transitions require strong internal electric fields within the semiconductor. It has been found that for most materials a threshold value of 3.3 kV/cm must be exceeded if oscillations are to take place. The mechanism responsible for the negative differential resistance in this device is a field-induced transfer of conduction band electrons from a low-energy, high-mobility valley to high-energy, low-mobility satellite valleys. The detailed description of this mechanism in pure semiconductors involves a knowledge of the band structure, the strength of interaction between electrons and phonons, and the phonon spectrum.

The most detailed theoretical treatments of the Gunn effect have relied heavily on Monte Carlo computer simulations of the electron dynamics involved. We too shall use the Monte Carlo technique to simulate the transient electron dynamics and to obtain the velocity-field curves for our purposes. A detailed discussion of this technique will be presented in the next chapter. For the present, we shall focus on the physics of the transferred electron effect and explain the mechanism responsible for producing the negative conductivity in GaAs.

2.2 Local Negative Conductivity in GaAs

Though GaAs represents a specific example, the transferred electron effect is similar in all direct band-gap materials. The current density in a semiconductor is proportional to both the density of electrons and their drift velocity. Consequently, a decrease in current density, with an increase in electric field, can be brought about by a decrease in either of these quantities. In the absence of traps and recombination centers,

a decrease in the drift velocity occurs in GaAs above a 3-kV/cm threshold field strength which reduces the current density. It is this mechanism that forms the basis of the Gunn effect, although that was not recognized at the time the effect was discovered. This decrease in drift velocity, in turn, is a result of the GaAs conduction band structure of GaAs as shown in Figure 2 [16].

GaAs is a direct-gap semiconductor with a conduction band minimum occurring at k=0, the center of the Brillouin Zone. The effective electron mass in this central valley is very low, being about 7 percent of the rest mass. Both of the above properties are essential ingredients of the Gunn effect. In addition to this central valley, GaAs possesses satellite valleys; that is, additional conduction band minima at energies much higher than the mean thermal energy kT. In the case of GaAs, the intervalley separation energy is about 0.29 eV. In the lowest valley, the effective electronic mass is small and the mobility μ_1 is high. Furthermore, the effective mass of electrons in the upper (satellite) valleys is higher and the mobility μ_2 consequently lower compared to the values in the central valley.

At room temperature, and in the absence of any strong electric fields, all electrons occupy the central valley, since the energy separation between it and the satellite valleys is much larger than kT. Because of the very low effective mass in the central valley, electrons are very easily heated up by an external electric field. When such heating takes place in response to applied bias, an increasing fraction of electrons are scattered into the satellite valleys as their energies begin exceeding the intervalley separation threshold. Upon scattering however, the larger effective mass causes a lowering of the mobility and

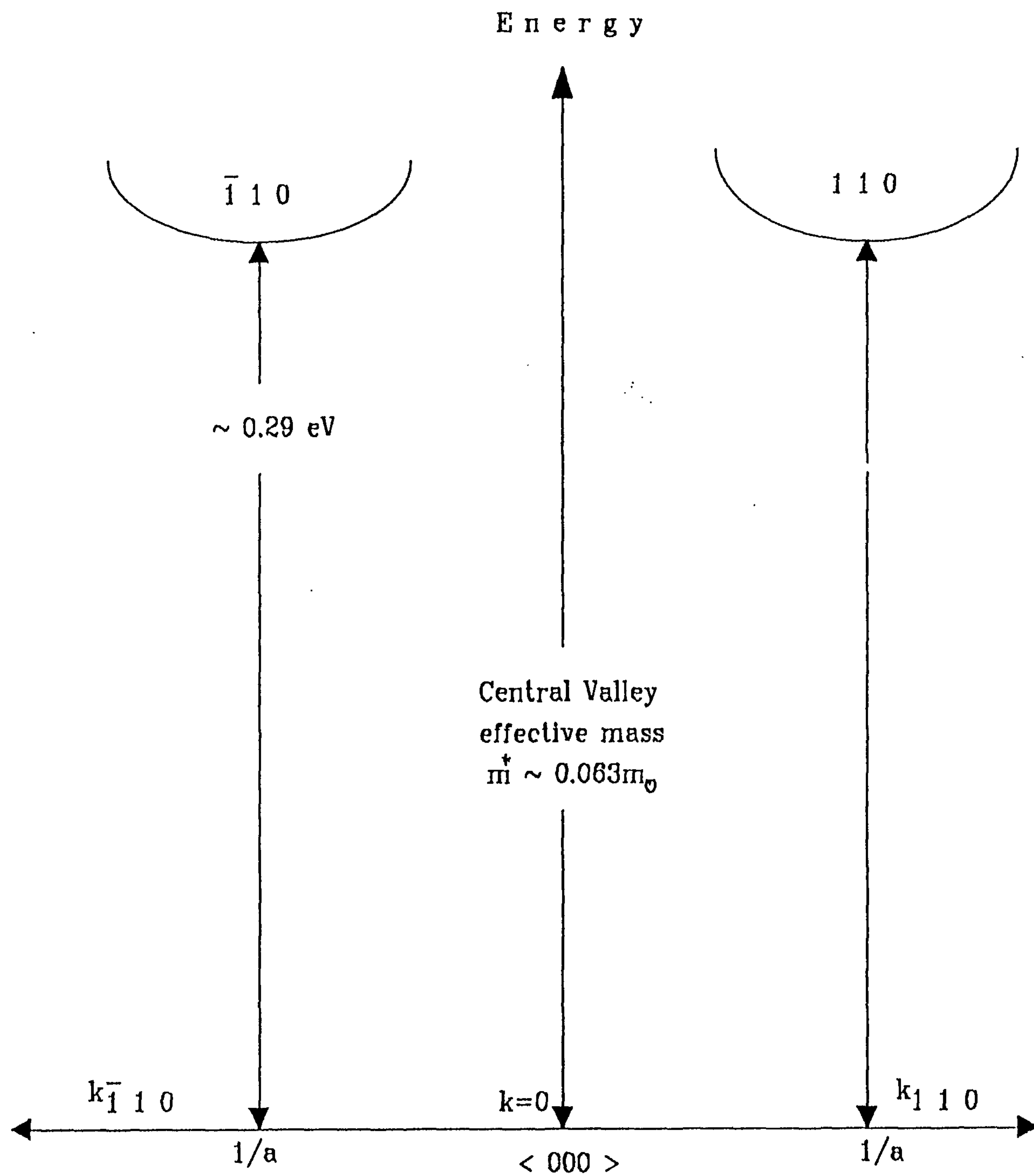

Figure 2. Conduction–band structure of GaAs

the overall electronic conductivity of the bulk semiconductor begins to decrease. A mathematical description of the development of this electron transfer effect will be presented next.

2.2.1 Development of the criteria for transfer

The electron drift velocity is given by $V_d = \mu E$, where E is the applied electric field. In the absence of spatially varying doping profiles, the current density reduces to:

$$J = neV_d = ne\mu E. \tag{2.1}$$

In a weak electric field at room temperature, all the electrons are in the lowest valley and current density roughly equals:

$$J = n_1 eV_1 = ne\mu_1 E\ , \tag{2.2}$$

since n_2, the concentration in the satellite valleys is negligibly small compared to the density n_1 in the central valley. Here, obviously $n = n_1 + n_2$ from particle conservation.

With an increase in the electric field, the kinetic energy of the electrons can reach and exceed 0.29 eV. Having exceeded the intervalley energy threshold, such electrons become available for being placed into any one of the six secondary minima through a phonon assisted collision process. In each of these secondary valleys, the electrons have a mobility μ_2 which is less than μ_1. As a result, the overall mobility on the average becomes:

$$\mu' = \frac{n_1\mu_1 + n_2\mu_2}{n_1 + n_2} . \quad (2.3)$$

while the current density is given as:

$$J = (n_1 + n_2)\mu' eE . \quad (2.4)$$

The conductivity of the device is then:

$$\sigma = e (\mu_1 n_1 + \mu_2 n_2) . \quad (2.5)$$

Differentiating the equation (2.4) with respect to the field, and making use of (2.5), one finally obtains:

$$\frac{1}{\sigma}\frac{dJ}{dE} = 1 + \frac{d\sigma/dE}{\sigma/E} . \quad (2.6)$$

For a negative resistance to exist, J must decrease with an increase in E and hence dJ/dE must be negative. This yields the following inequality:

$$-\frac{d\sigma/dE}{\sigma/E} > 1 . \quad (2.7)$$

Assuming that the mobilities μ_1 and μ_2 are proportional to E^p (with p being constant), the field dependent changes in the mobility can be expressed as:

$$\frac{d\mu}{dE} = kpE^{p-1} = \frac{p\mu}{E} . \quad (2.8)$$

Using equation (2.8) in (2.7), the necessary condition for negative differential conductance can finally be expressed as:

$$[(\frac{\mu_1 - \mu_2}{\mu_1 + (n_2/n_1)\mu_2})(-\frac{E}{n_1}\frac{dn_1}{dE}) - p] > 1 \ . \qquad (2.9)$$

In order to satisfy the above condition, the following criteria become necessary:

(a) the term p, which is the exponent in the expression linking μ and E, must be negative. Such indeed is the case over section 2 of the velocity-field curve shown in Figure 3.

(b) The term dn_1/dE must be negative. This is the intervalley transfer function for the electrons and depends on the free electron density, the operating temperature and the intervalley energy difference.

(c) The first term must be positive: that is μ_1 must have a greater magnitude than μ_2, a condition which initiates the transfer.

Most of the III-V compounds (eg. InP, InAs, GaP, GaAs, InSb...) satisfy these criteria, whereas silicon and germanium do not [17]. Furthermore, as GaAs technology is relatively better developed than for the other materials, Gunn diodes are usually fabricated from this material.

Similar behavior is to be expected for any other semiconductor having a similar band structure; namely, a low-mass central valley combined with a set of high-mass satellite valleys. Prerequisites also include an energy separation between the high - and the low-mass valleys larger than kT, but smaller than the energy gap of the semiconductor. The latter is necessary to avert the possibility of avalanche breakdown before the initiation of the intervalley transfer process.

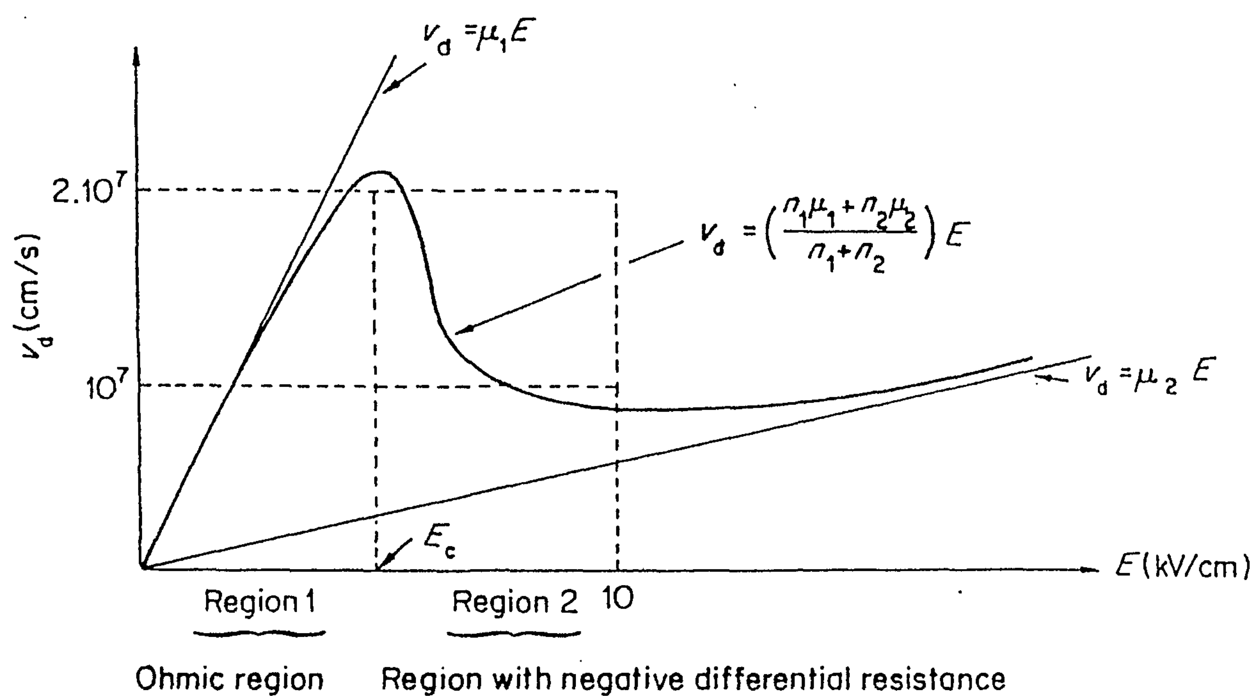

Figure 3. Curve of velocity against electric field for carriers in GaAs.

To summarize the processes described in this section, a semiconductor material in general must fulfill the following requirements in order to be suitable for the electron-transfer mechanism and, hence, to show an negative differential conductance region:

1. The conduction band must have a many-valley structure with the curvature of a valley 1 exceeding that of a valley 2 ($m^*_2 \geq m^*_1$).
2. The less curved valley 2 must be positioned higher in energy by a few kT than valley 1 in order to be essentially depopulated in the field-free case.
3. Additionally, to prevent impact ionization from setting in before the electron transfer commences, the ionization energy must exceed the separation of the valley minima.

2.3 The operating modes of Gunn devices

In this section, we begin with a brief review of the early-stage space-charge growth for a device with negative differential mobility. The goal is to demonstrate that spatially heterogeneous charge distributions are necessary for microwave oscillations. Finally, for completeness, we shall outline some common modes of device operation.

2.3.1 Space-charge growth mechanism

A semiconductor exhibiting bulk negative differential resistivity (NDR) is inherently unstable, because a random fluctuation of carrier density at any point in the semiconductor produces a momentary space charge that grows exponentially in time. The one dimensional continuity equation is given by:

$$\frac{\partial n}{\partial t} + \frac{1}{q}\frac{\partial J}{\partial x} = 0. \qquad (2.10)$$

where

$$J = \frac{E}{\rho} - qD\frac{\partial n}{\partial x} \quad , \qquad (2.11)$$

with ρ being the resistivity and D the diffusion constant. A small fluctuation of the majority carriers from the uniform equilibrium concentration n_o, creates the local space-charge density of $(n - n_o)$ and leads to electric field gradients. These gradients are quantitatively expressed through the Poisson equation as :

$$\frac{\partial E}{\partial x} = \frac{q(n - n_o)}{\epsilon_s} \quad , \qquad (2.12)$$

where ϵ_s is the dielectric permittivity. By solving the above set of equations, one obtains the temporal response solution as:

$$n - n_o = (n - n_o)_{x=0} \exp(-t/\tau_r) \; , \qquad (2.13)$$

where τ_r is the dielectric relaxation time given by

$$\tau_r = \rho\epsilon_s = \epsilon_s/q\mu n \approx \epsilon_s/q\mu n_o \qquad (2.14)$$

This time constant represents the decay of the space-charge to neutrality if the differential resistivity is positive. However, if the semiconductor exhibits a negative differential resistivity, any charge imbalance grows with a time constant equal to $|\tau_r|$ instead of exhibiting a decay [18].

Hence, if the above (eqn 2.14) relationship remained valid throughout the entire transit time of the space-charge layer, the maximum growth factor would be $\exp(L/v|\tau_r|)$, where L is the length of the device, and v is the average drift velocity of the space-charge layer. For large space-charge growth, this growth factor must be greater than unity, making $L/v|\tau_r| > 1$, or $n_oL > \varepsilon_s v/q|\mu_-|$. For n-type GaAs and InP, the above inequality works out to be: $n_oL > 10^{12}$ cm^{-2}. The transferred electron devices with n_oL products smaller than 10^{12} cm^{-2} have a stable field distribution and exhibit a different mode of operation.

Because of this negative differential resistivity, the semiconductor, initially homogeneous, becomes electrically heterogeneous in an attempt to reach stability. We present next a simple argument to show that for voltage controlled NDR devices, high-field domains (or an accumulation layer) will form [19]. The simple argument will be modified when we discuss the various other modes of operation in the latter part of this section.

To consider in more detail the space-charge instability [20] of a voltage controlled NDR, we refer to Figure 4. Figure 4a shows a typical instantaneous J-E plot and Figure 4b shows the charge profile of this device. Assume that at point A in the device there exists an excess (or accumulation) of negative charge that could be due to a random noise fluctuation or possibly nonuniformity in doping (Figure 4c). Figure 4d shows the electric field distribution, where the field to the left of point A is lower than that to the right of A. If the device is biased at E_a on the J-E curve, this condition would imply that the carriers (or current) flowing into point A are greater than those flowing out of point A,

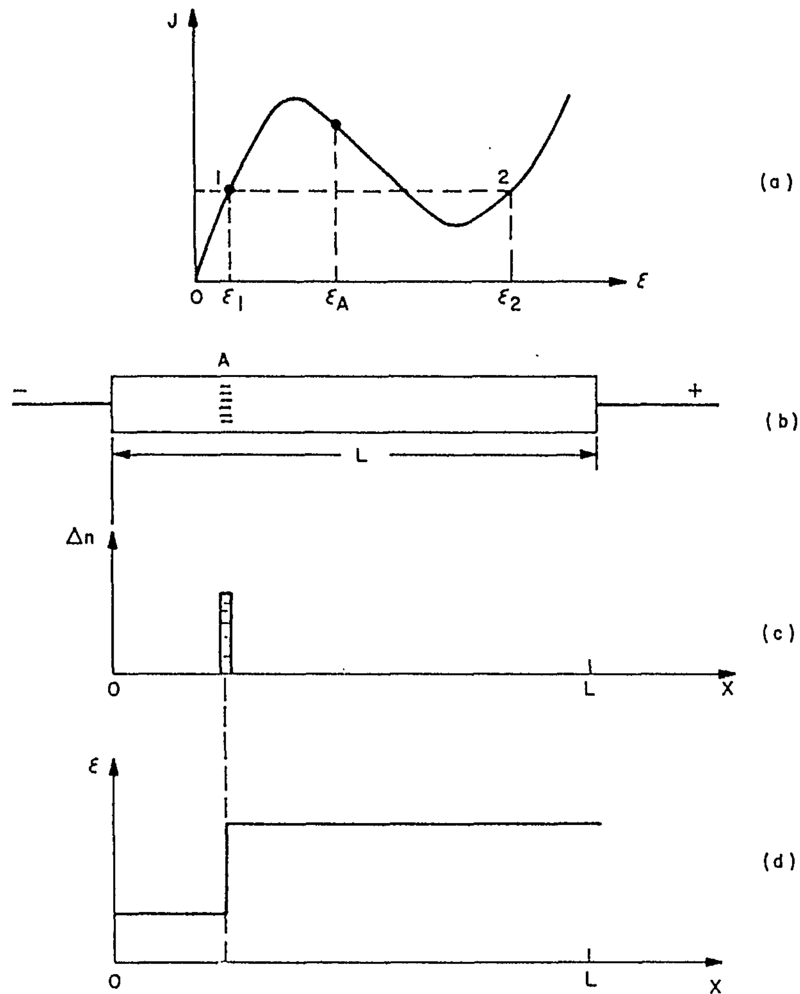

Figure 4. Formation of electron accumulation layer in a perturbed medium of negative resistivity a) current density-electric field plot, b) charge profile of the device, c) fluctuation of doping, d) electric field distribution

thereby increasing the excess negative space-charge at A. This reduces the field to the left of point A even below its original value, while the field to the right becomes higher than before. The overall results in an even greater space-charge accumulation. This process continues until the high and low fields both obtain values outside the NDR region and settle at points 1 & 2 in Figure 4a with the common current value. The net result is a formation of a traveling space-charge accumulation layer. Quite obviously, the above process successfully occur only on the condition that the electronic density inside the crystal is large enough to allow for the space-charge to build up during its transit time.

The pure accumulation layer discussed above is the simplest form of space-charge instability. When there are positive and negative charges separated by a small distance, one has a dipole formation (or domain) as shown in Figure 5. The electric field inside the dipole is greater than the fields on either side of it, Figure 5c. Because of the negative differential resistance, the particle current in the low-field region is consequently larger than that in the high-field region. The two field values will tend toward equilibrium levels outside the NDR region, as shown in Figure 4a. The dipole has now reached a stable configuration. The dipole layer moves through the crystal and disappears at the anode, at which time the field begins to rise uniformly across the sample through threshold; that is, $E > E_t$, as shown in Figure 5a. A new dipole layer then forms, and the process repeats itself. We shall now consider a few of the important operation modes.

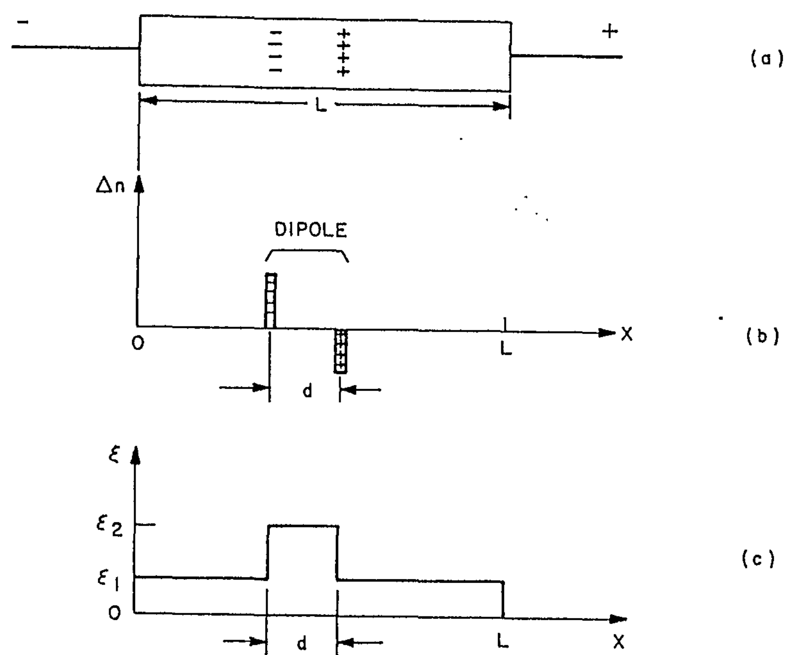

Figure 5. Formation of electron dipole layer in a perturbed medium of negative resistivity a) charge profile of the device, b) fluctuation of doping, c) electric field distribution

2.3.2 Modes of Operation

Since Gunn first observed oscillations in a GaAs rod, several operating modes have been studied. We are concerned with the Gunn and the LSA (Limited Space-charge Accumulation) modes. The Gunn mode in turn is subdivided into: (i) Accumulation Layer Mode; (ii) the Transit-time or Fundamental Mode; (iii) the Quenched Mode; and (iv) the Delayed Mode [21].

Of these, the accumulation layer mode is characterized by an n_0L product value of less than 10^{12} cm^{-2}. The device doping levels and the transit lengths are inadequate for the space-charge growth to stabilize. A continually growing accumulation layer propagates towards the anode. This in turn causes a time-dependent variation in the internal electric field as shown in Figure 6 [22]. The net integral of this field curve, however, remains constant for a steady state DC bias voltage.

The Transit-time Dipole Layer mode of operation is made possible in a device if the n_0L product exceeds 10^{12} cm^{-2}. This mode is characterized by a stable dipole layer containing a high-field region, which neither grows nor shrinks with time. The high field domain is nucleated close to the cathode and travels the full length of the sample to the anode. The frequency of operation is then controlled by the transit time and hence is inversely dependent on the device length.

In the Quenched Dipole Layer mode, the device operates at frequencies higher than those made possible from the transit time concept. In this mode, the device behavior is controlled through an external resonant circuit which effectively sets the voltage across the device. As the voltage begins to decrease in response to the circuit oscillations, the

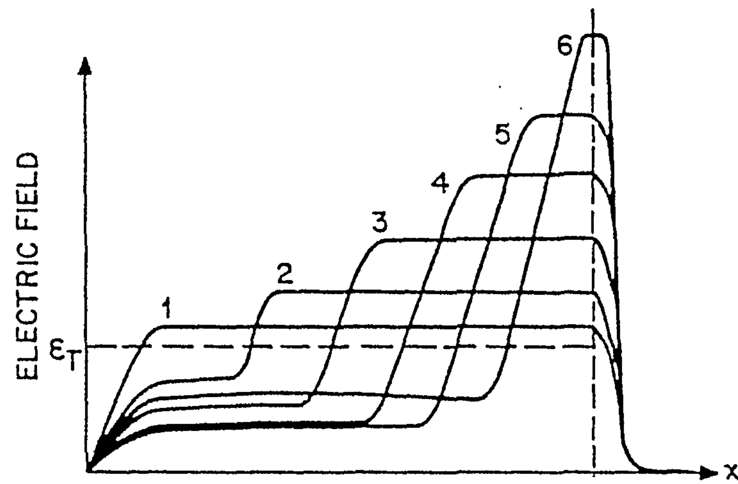

Figure 6. Time dependent variation of internal electric field across the Gunn device.

internal dipole width shrinks, until it is completely quenched. As a result, the overall result traversed by the dipole domain is less than the total device length.

Finally, in the Limited-Space-Charge Accumulation (LSA) Mode of operation, the electric field across the device rises from below the threshold value and falls back again so quickly that the space-charge distribution associated with high-field dipole-layers does not have sufficient time to form. Only a primary accumulation layer forms near the cathode; the rest of the device remains fairly homogeneous, provided that the doping fluctuations are sufficiently small to prevent the formation of dipole-layers. Under these conditions, a large portion of the device exhibits a uniform field, and the power generation at the circuit-controlled frequency is affected by the negative differential mobility of individual electrons rather than by the movement of space-charge bunches.

2.4 Schemes for Improving Device Performance

So far, we reviewed the physical characteristics of Gunn devices and mainly assumed that the device were made from GaAs. In this section, we discuss the use of alternative heterojunction structures and different semiconductor materials, to improve the high frequency device performance.

Usually, Gunn devices are associated with a dead zone. This is a characteristic distance that the electrons have to traverse before they can acquire sufficient energy from the applied electric field and attain the threshold velocity. The dead zone serves no useful purpose and delays the generation of microwave power. The situation becomes more acute for high frequencies which require shorter transit lengths. These size reductions worsen

the situation since the relative percentage of the dead zone gets larger. In addition, the temperature variations also have an adverse effect on the dead zone formation. Typically temperature fluctuations alter the phonon populations within the device and bring about changes in the intervalley phonon-assisted transfer. The net result of this temperature dependence of the intervalley dynamics is a degradation in the device performance and enhanced uncertainity in the successful growth and formation of the instability [23].

In order to overcome these drawbacks of device scaling at high frequencies, one needs to set up schemes for reducing and stabilizing the dead zone. The simplest method for doing so involves the use of alternative semiconductor materials that have a smaller electronic mass and/or intervalley transfer threshold energy. This scheme however, is not always feasible since the semiconducting material may not simultaneously have a low electronic mass and intervalley separation. For example, InAs has a lower effective mass than GaAs but a much higher value of $E_{\Gamma\text{-}L}$. Furthermore, technological difficulties may prevent a successful device fabrication.

The above difficulty can however, be overcome through the use of alternative heterostructures, formed by joining dissimilar semiconductors. The basic concept is to use differences in the bandgaps of two semiconductors placed adjacently for creating energetic hot electron conditions. The cathode region is typically fabricated from a wide bandgap material and acts as the "hot electron injector". The middle drift region has a lower bandgap and comprises the main transit region, as shown later in Figure 34. The difference in the electronic band offsets caused by the dissimilar bandgaps is used to convert the potential energy at the cathode into large kinetic energy in the drift region.

Electrons are therefore, propelled into a high energy state as they begin their transit. The $Al_xGa_{1-x}As$ - GaAs combination shown is typically used because the technology is well developed, and the material system can be fabricated without excessive lattice mismatch.

The limitations to the microwave power obtainable from Gunn oscillators are a result of the heating of the device and the dielectric breakdown field of bulk GaAs. Any heating effects which can be removed will add to both the power and the efficiency. Ondria and Ross [24] have shown that by grading the doping profile in the transit region of a conventional Gunn diode, it is possible to improve the diode's performance. The attraction of varying the doping in the transit region in a logarithmic manner from high at the cathode to low at the anode, is that the electric field throughout the transit region is much more uniform when the device is operated. This reduces excessive heating of electrons by the field near the anode and leads to a higher efficiency.

CHAPTER 3

NUMERICAL SIMULATION SCHEME FOR THE GUNN DIODE

In chapter 2, we have discussed the transferred electron effect, examined the implications for microwave oscillators, and outlined the role of intervalley scattering. The physical phenomenon is clearly controlled by the complex, time-dependent dynamics involving carrier-phonon scattering processes. For an accurate description of a Gunn diode microwave oscillator, one must correctly model the internal device physics and the circuit response jointly. Though a number of alternative techniques such as analytical solutions of the Boltzmann Transport Equation [25] and iterative schemes [26] are available, we have chosen to use the Ensemble Monte Carlo method. This method is easy to implement and offers the following advantages:

1) Stochastic calculation is achieved at minimum level of difficulty while incorporating memory effects.
2) Time- and space-dependent phenomena can be easily simulated.
3) The microscopic interpretation of the physical details is quite transparent.
4) No arbitrary assumption regarding the distribution function needs to be made.
5) The analysis can be extended to fluctuation phenomena and hence noise properties can be calculated.
6) Many-body carrier-carrier effects can be included self-consistently.

These advantages account for the popularity of the Monte Carlo method, which at present is more widely in use for device simulations than any other technique.

In this chapter, the entire numerical scheme for Gunn diode simulation is outlined. Specifically, we begin with a detailed description of the Monte Carlo technique in section 3.2. In section 3.3, the numerical formulation and implementation of Poisson's equation is discussed. Finally, the results obtained from Monte Carlo calculations of the velocity-field curve are presented in section 3.4., which demonstrate a successful implementation of the entire procedure.

3.1 Monte Carlo Simulation

The Monte Carlo method has become a standard numerical method of simulating electron and hole transport in semiconductors. It is based on the approach developed by Kurosawa (1966) [27]. The idea of this technique is to simulate electron motion both in real and **k**-space using random numbers to account for carrier dynamics at the microscopic level. The overall motion is comprised of free electron flights that are being continually interrupted by scattering processes, resuming each time from a new starting point in **k**-space. The time duration between two successive collisions and the choice of the scattering events involved are selected stochastically in accordance with some given probabilities describing the microscopic processes. During the free flight, carriers obey classical laws of Newtonian mechanics. The collisions or scattering events occur randomly in real space and are unique functions of the carrier energy. The final state of carriers

after a collision is determined by a selection procedure in accordance with energy and momentum conservation, and is implemented by using additional pseudorandom numbers.

The schematic flow-chart of the Monte Carlo program is shown in Figure 7. Under the influence of an electric field, electrons will be accelerated until they scatter. The scattering probability at any time is given as:

$$p(t) = \lambda[k(t)] \exp \left[-\int_{0}^{t} \lambda(k(t'))dt' \right] , \tag{3.1}$$

where $\lambda(k)$, the total scattering rate, is a complicated nonlinear function of energy. The argument "k" in the above equation is the wavevector and related to the carrier energy as:

$$(1+\alpha E)E = \frac{\hbar^2 k^2}{2m} , \tag{3.2}$$

where α describes the non-parabolicity of the band-structure. Evaluation of the scattering probabilities from equation (3.1) is non-trivial. Rees[28], however, developed a very simple method to overcome the difficulty of evaluating the time-dependent integral. He introduced a fictitious term called "self scattering" to make the total scattering rate constant and equal to Γ. Under this scheme, the final state k' for carriers undergoing such a self scattering is taken to equal its state k before the collision; so that in practice the electron motion continues unperturbed as if no scattering had occurred at all. With the implementation of such a self-scattering, equation (3.1) becomes:

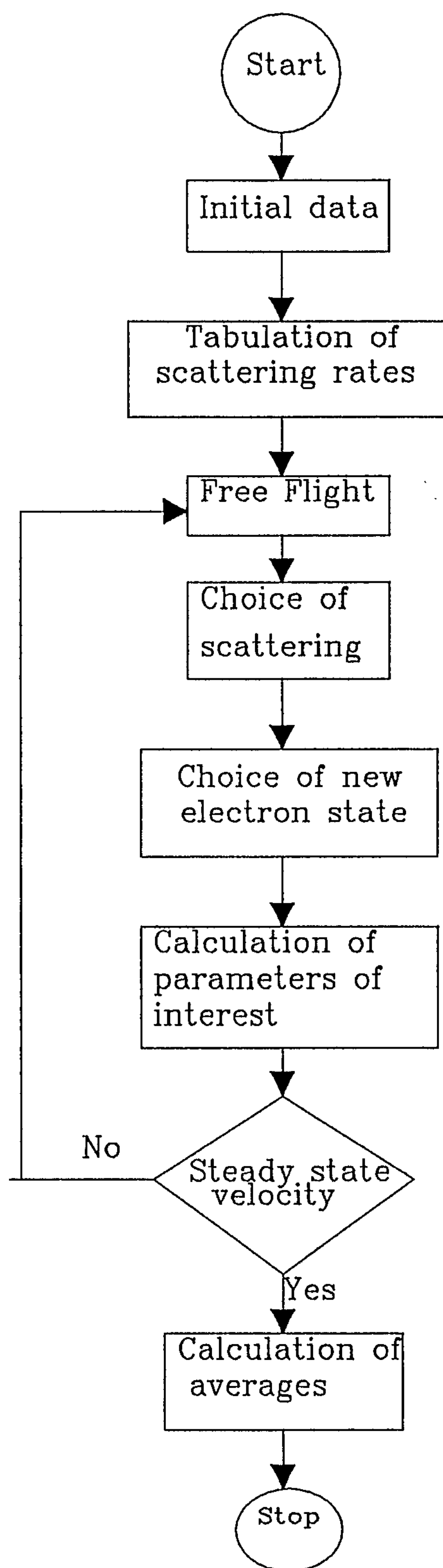

Figure 7. Flow–chart of the Ensemble Monte Carlo program

$$P(t) = \Gamma \exp[\ -\Gamma\ t]\ , \tag{3.3}$$

Since the cumulative probability distribution function at any time "t" is given in terms of a number r between 0 and 1 as:

$$r = \int_0^t p(t')\, dt'\ , \tag{3.4}$$

substitution of equation (3.3) into (3.4) yields:

$$r = \int_0^t \Gamma \exp(-\Gamma t')\, dt' = 1 - \exp(-\Gamma t)\ . \tag{3.5}$$

As a result, the random free flight times work out to be:

$$t_r = -\ln(\ 1 - r) / \Gamma = -\ln(\ r\ ) / \Gamma\ . \tag{3.6}$$

In the above equation, ln(1-r) and ln(r) are equivalent, since r is a uniformly distributed variable. During free flight, carrier momentum is continually updated through:

$$k(t_o + t_r) = k(t_o) + \frac{qE}{\hbar}\, t. \tag{3.7}$$

where $k(t_0)$ and $k(t_0+t_r)$ are values of the electronic wavevector before and after the free flight which lasts a time t_r. Also, E is the applied electric field and, q is the electronic charge. Once the free flight is terminated at the time instant ($t_0 + t_r$), an appropriate scattering process has to be selected. This is again done stochastically by generating a random number r_2 between 0 and Γ, and testing the inequality:

$$r_2 < \sum_{j=1}^{m} \lambda_j(k) , \tag{3.8}$$

for all m. The subscript j = 1,2,...,m goes over the various scattering mechanisms including the self-scattering process.

Figure 8 shows how a scattering event is determined based on its probability of occurrence. A low scattering rate λ_1, would not be chosen often through this procedure, since the probability of generating a very low random number would be small. It may noted that, since the scattering rates are all independent of each other, the introduction of self scattering does not affect the other rates.

Once the scattering mechanism at the end of the electron free flight has been determined, the new state characterized by a different set of energy and momentum values has to be chosen. This final state uniquely depends on the type of scattering process involved in transferring the electron to its final state. If the free flight ended with a self-scattering, k' must equal k, since both the momentum and the energy of the carrier remain unchanged. For either ionized impurity scattering or acoustic scattering, the initial energy equals the final energy because of the elastic nature of collision. The wavevector k, however, is randomized by the process. Optical phonons extract or add a constant quanta of energy $h\omega_0$ through emission or absorption. Such a fixed energy quanta is a direct consequence of the ω-k dispersion curves for optical phonons in semiconducting materials.

After undergoing a scattering event, the carriers begin their next flight, and the drift-scatter mechanism is continuously repeated until the end of each time step T_s. The

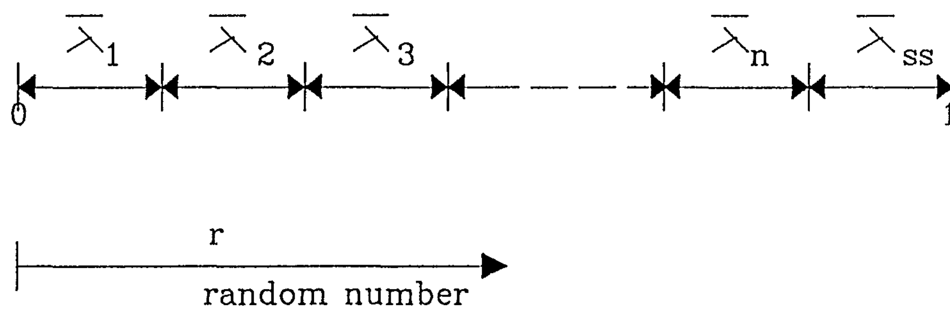

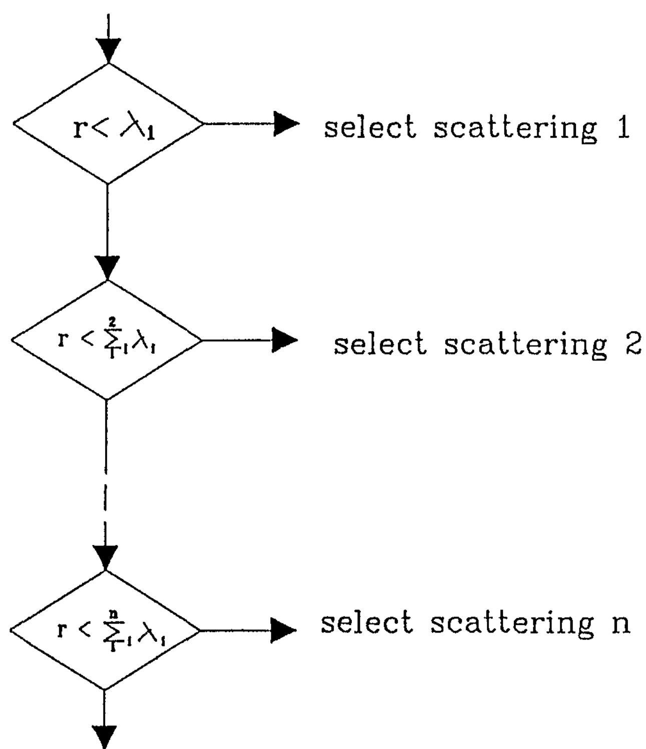

Figure 8. Flow–chart of scattering selection in Monte carlo simulations.

ensemble averages of all the quantities of interest such as drift velocities, particle currents, etc., are then calculated at each time step. The value of the drift velocity V(t), for example, is the ensemble average at time t over the N carriers in the simulation. It is given by :

$$V(t) = \frac{1}{N} \sum_i V_i(t) , i = 1, 2, 3, ..., N . \tag{3.9}$$

The repetitive procedure of collective drift and subsequent scattering continues until the end of the total simulation time.

In order to uniquely simulate a given semiconductor, the Monte Carlo method uses a set of material parameters. The parameters used in this thesis to model electronic transport in GaAs are shown in Tables I and II. This set of parameters was chosen based on published work in the literature and yields a good fit of the velocity-field characteristics with experimental observations [29].

3.2 The solution of Poisson's Equation

The need to solve Poisson's equation arises, because one requires full knowledge of both the internal electric field and the device potential at every time instant. The spatial distribution of mobile charge and the ionized doping atoms is, in general, not homogeneous within the simulated device. Such inhomogeneity gives rise to non-uniform electric fields which work to re-distribute the mobile charge. Ensuing changes in the carrier positions, in turn, modify the electric field distributions within the device. As a result, a self consistent procedure must be adopted, to update the electric field at periodic

Table I. Properties of Gallium Arsenide at 300 K

Property	Value
Atoms/cm^3	4.42×10^{22}
Atomic Weight	144.63
Density (g/cm^3)	5.37
Energy-band gap	1.43
Dielectric constant (High-frequency)	10.92
Dielectric constant (Low-frequency)	12.92
Intrinsic carrier concentration	1.79×10^6
Lattice constant	5.6533 A°
Melting point	1238°C
Mobility (electrons)	8500 cm^2/V-sec
Breakdown Field	$\sim 4 \times 10^5$ V/cm
Intervalley Phonon	
energy (eV)	0.0311
Heavy-hole mass	0.45
Light-hole mass	0.082

Table II. Material parameters for GaAs Monte Carlo Program

Parameter		Γ	L	X
Number of Valleys		1	4	3
Effective mass ratio		0.063	0.222	0.580
Nonparabolicity factor (eV^{-1})		0.61	0.46	0.20
Valley separation from Γ valley (eV)			0.29	0.49
Polar optic-phonon energy (eV)		0.0364	0.0364	0.0364
Acoustic deformation potential (eV)		7.0	7.0	7.0
Coupling constant (10^8 eV/cm)	Γ to		7	10
	L to	7	10	5
	X to	10	5	10

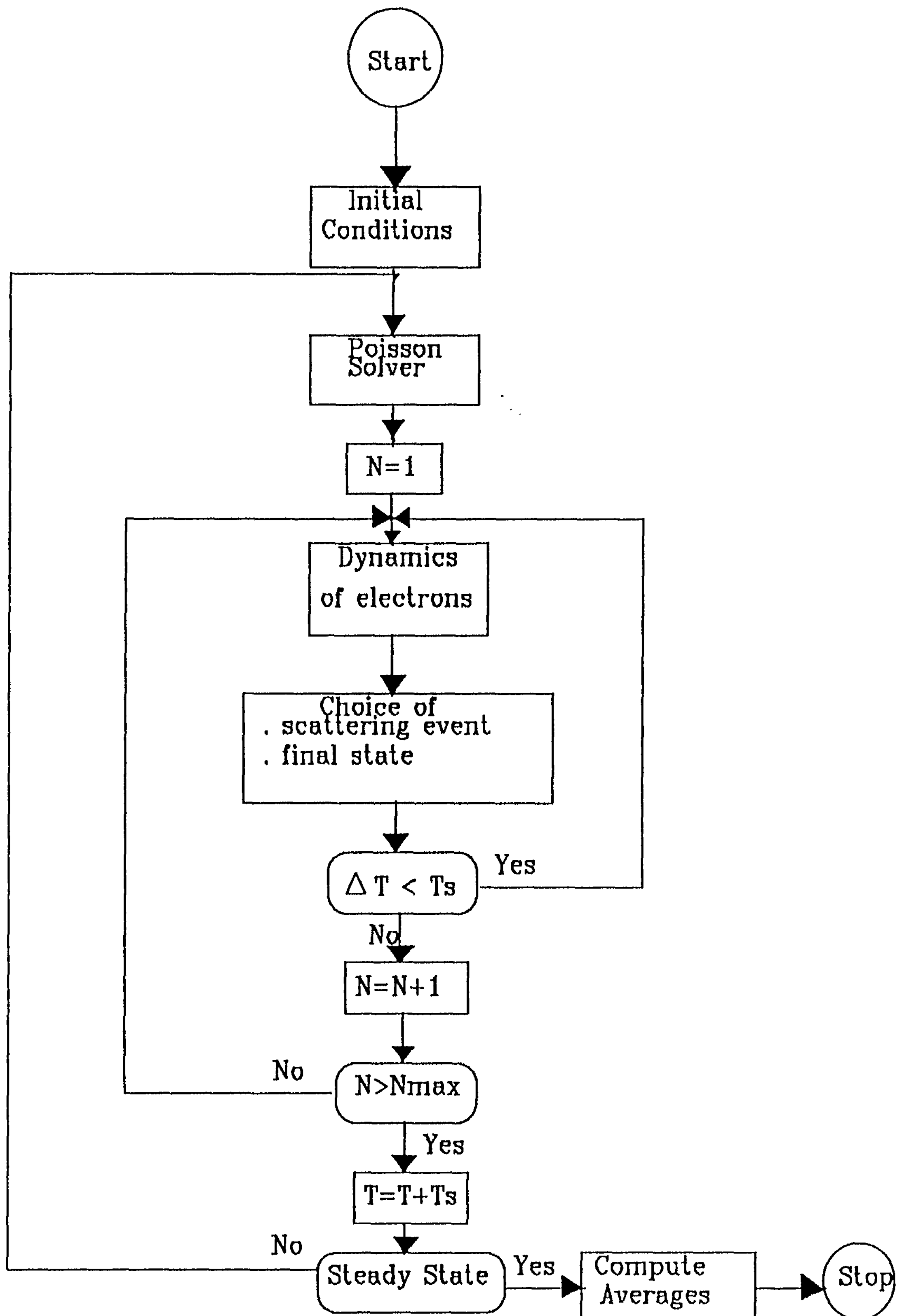

Figure 9. Flow–chart of a device Ensemble Monte Carlo Program

intervals through a new solution of Poisson's equation. Charge flows must be monitored, in addition to calculating carrier dynamics in response to local fields at any time. The flow-chart in Figure 9 shows a general self-consistent Ensemble Monte Carlo algorithm.

An initial distribution of position and momentum of the electrons inside the device is set up at the beginning which defines the initial conditions. The starting electric field distribution is obtained through a solution of Poisson's equation. This dictates the dynamics of all the electrons in the ensemble which are simulated in parallel for a chosen time step T_s. During this time interval, scatter and drift occurs continuously, and possible interactions with the boundaries are monitored. At the end of a time step, the new charge distribution is set up through a knowledge of free carrier positions. Poisson's equation is subsequently solved once again to update the internal field distribution, and these self consistent iterations are continued after every time step until the end of the simulation. The time T_s between two successive solutions of the Poisson's equation obviously has to be considerably less than the dielectric relaxation time.

The simulation of both transient and steady state phenomenon is of particular interest for the analysis and modeling of semiconductor devices. In the case of a device, the electrons are constrained inside the device space which represents an open system through which particles flow. This flow of charge is clearly controlled by, and dependent on the boundary of the system and so appropriate boundary conditions on the sides must be adopted. We model the contacts as being Ohmic in nature with an abundant supply of free carriers. Consequently, when a particle crosses one of these boundaries, we reinject

another particle with the same axial momentum through the other side to maintain current continuity (periodic boundary conditions).

In order to implement and test a Poisson solver within the Monte Carlo program, a test device structure was chosen. The geometry of the device considered in the simulations is shown in Figure 10. The total length was about 2.0 microns, divided into three n^+,n and n^+ regions, of lengths 0.2, 1.6, 0.2 microns, respectively. The choice of this structure is to purposely bring about charge non-uniformities which lead to spatially non-uniform built-in electric fields. Both the width and height of the device were taken to be 1 μm. Poisson's equation, was solved by the method of finite differences, as this method is the least expensive computationally, and relatively easy to implement. Though, in general, Poisson's equation must be solved in three-dimensions, the transverse symmetry inherent in the chosen device structure, allows the reduction to a one-dimensional problem.

The one-dimensional Poisson's equation is written as:

$$\frac{\partial^2 \phi}{\partial x^2} = q\,(n - N)/\epsilon\ , \tag{3.10}$$

where ϕ is the potential, n the free carrier concentration, N the donor impurity doping which is a function of position in this case, q the electronic charge, and $\in$ the dielectric constant. On discretizing Poisson's equation using finite differences over a uniform mesh, we get

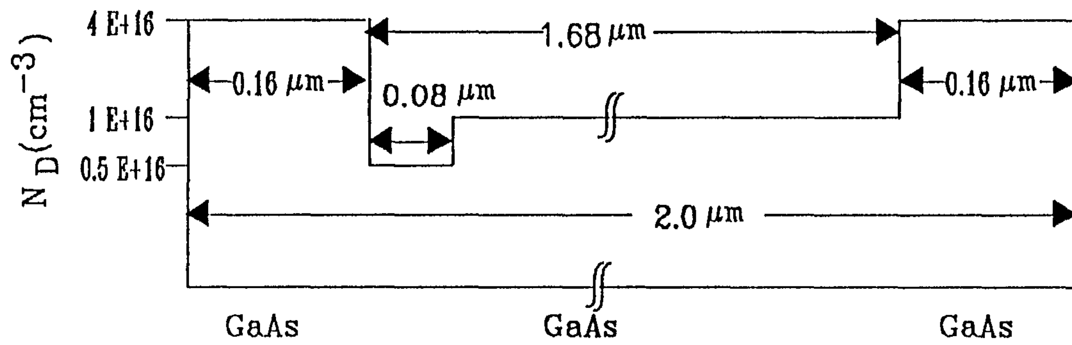

Figure 10. The doping profile of the simulated device structure for GaAs notch oscillator

$$\phi^{j+1} - 2\phi^{j} + \phi^{j-1} = q(\Delta x)^2(n^j - N^j)/\epsilon , \tag{3.11}$$

where Δx is the grid spacing. The uniform mesh spacing was chosen for computational convenience and allows a simple but efficient scheme for the assignment of charge at various nodes. In order to actually solve Poisson's equation, the charge density at various nodes of the grid generated across the device, needs to be determined. Since the ionized donors are immobile, they present a uniform background of positive charge in the dopedregions of the chosen test device. The electrons on the other hand, were initially distributed in accordance with the doping density. Their subsequent changes in position with time were due to the Ensemble Monte Carlo dynamics. Equation (3.11) was solved on the IBM 3090, using a tridiagonal matrix solver. The electric field values were obtained from the potential vector by finite differencing, and used for updating charge movement during the subsequent time steps.

By repeatedly applying the above method, the results for the electronic distribution, the electric field, and potential profiles throughout the device were obtained for zero-bias conditions. These are shown in Figures 11 to 13. In agreement with the depletion approximation theory, Figures 12 & 13 show the internal electric field and potential along the device, under zero-bias conditions.

3.3 Velocity-Field Curve

In the preceding sections, a discussion of both the Monte Carlo procedure and numerical implementation of Poisson's equation has been given. The role of non-uniformities in setting up internal fields has also been demonstrated. In this section, we

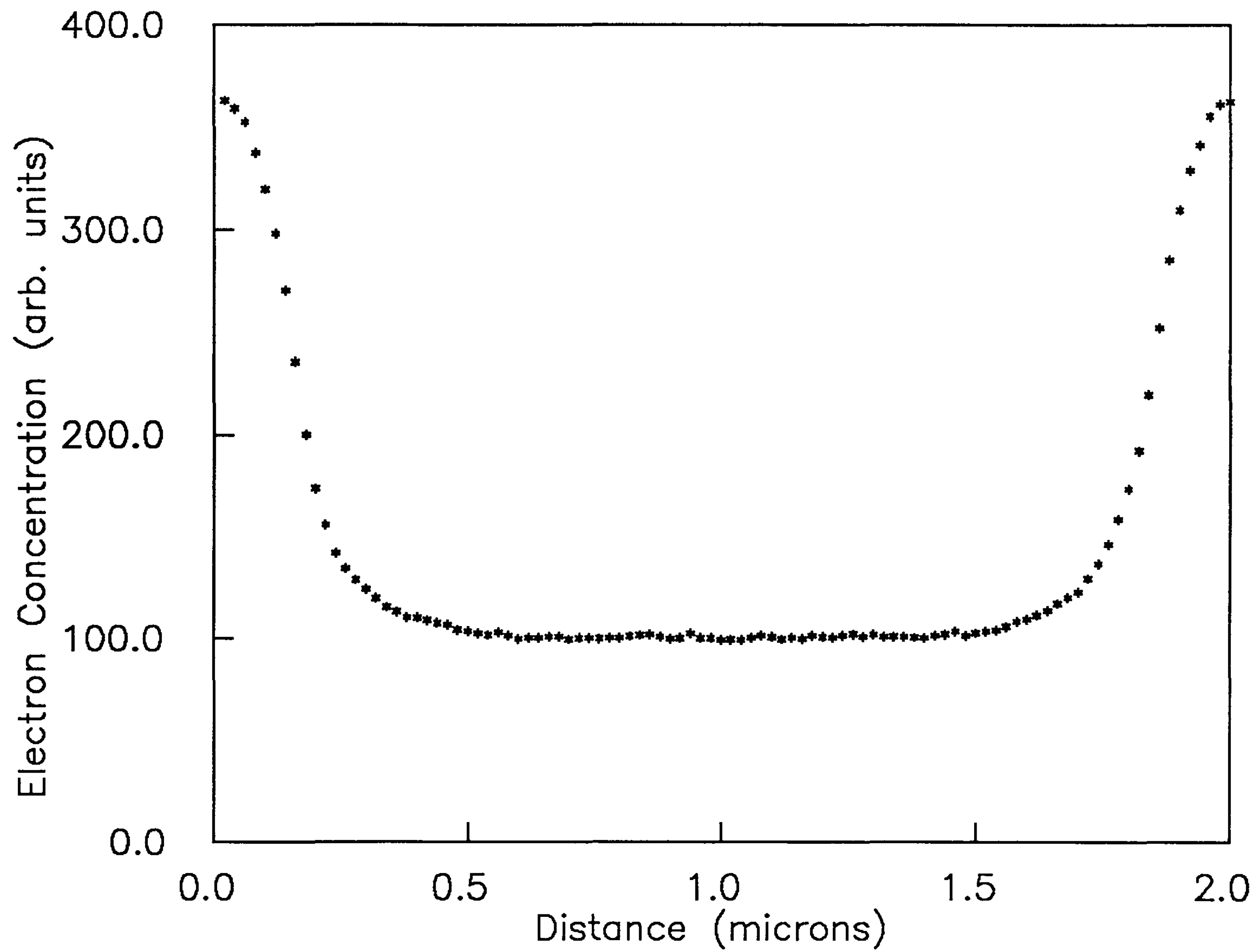

Figure 11. Electronic distribution profile throughout the device under zero-bias conditions.

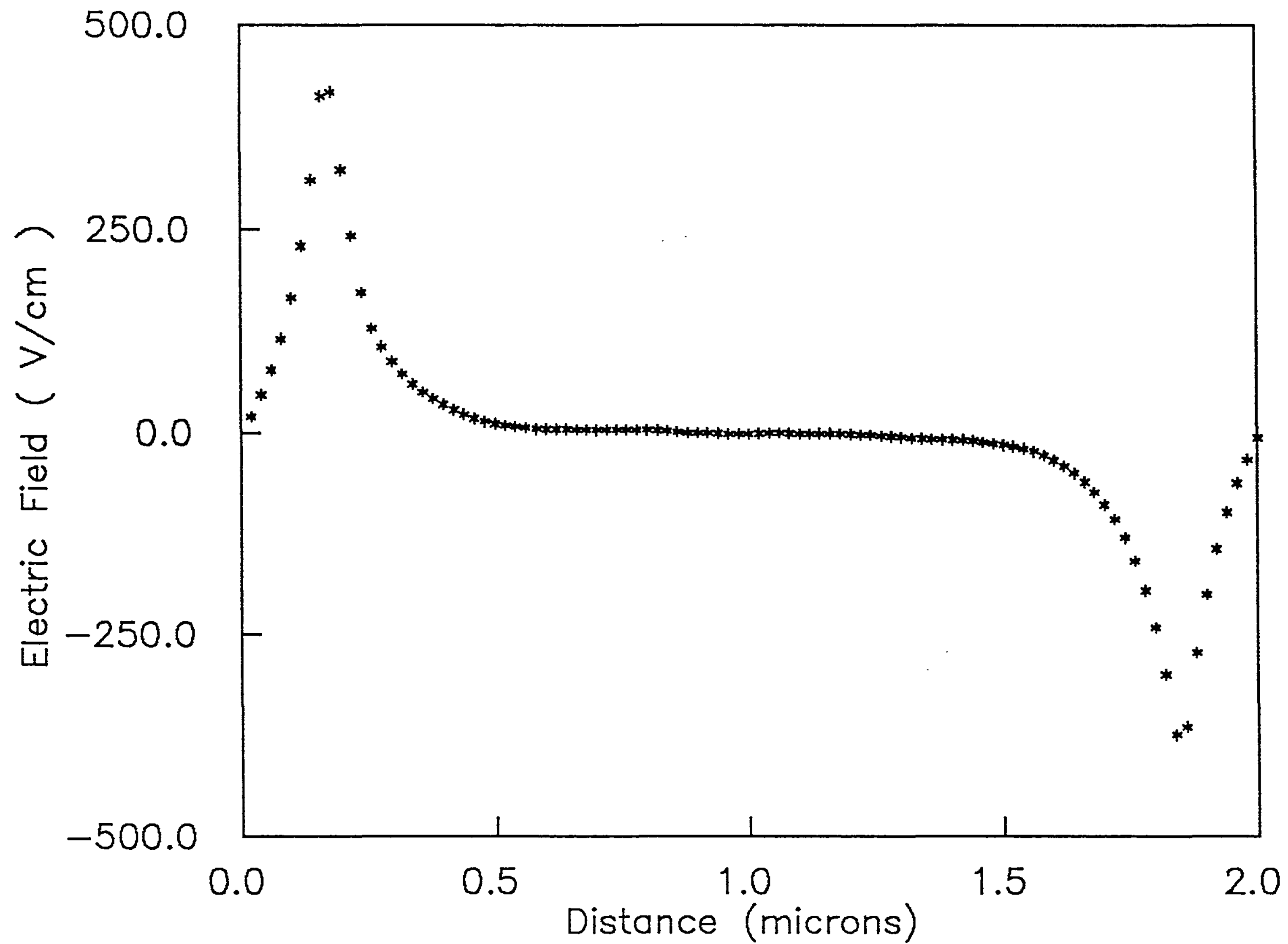

Figure. 12 Electric field distribution profile throughout the device under zero–bias conditions.

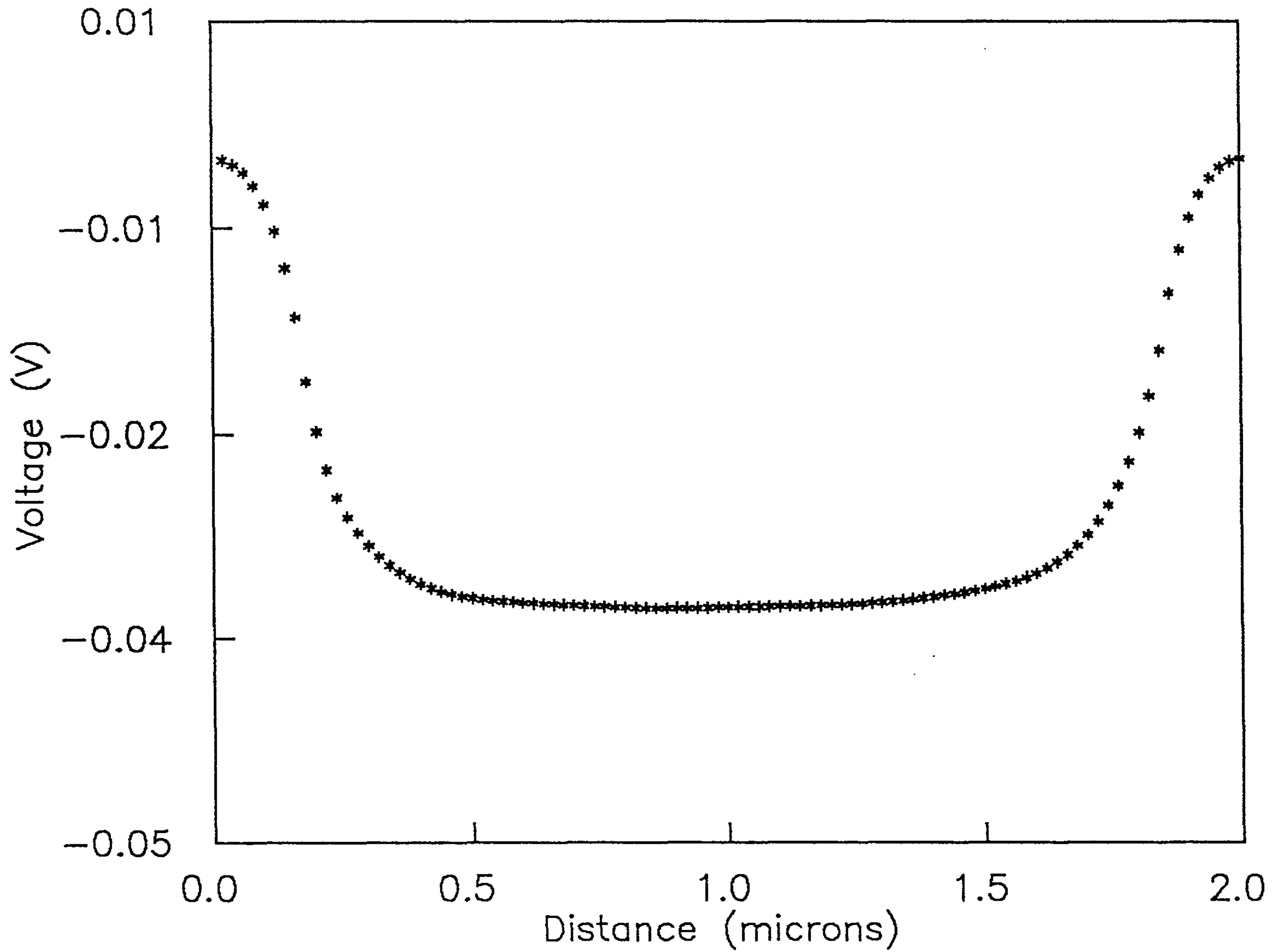

Figure 13. Voltage profile across the device under zero−bias conditions

focus on carrier transport and test the field- dependent velocity response in GaAs through Monte Carlo simulations. For this purpose four different electric fields of 2, 5, 10, and 20 kV/cm were considered. Figure 14 shows a transient velocity curves at 10, and 20 kV/cm and a very fast rise is obtained. This is expected since the electrons are initially in the lowest, high mobility Γ valley at room temperature. Under the influence of the electric field, however, these electrons gain energy and accelerate causing the velocity to increase. Once they attain energies higher than the energy threshold, they undergo intervalley scattering into the higher mass satellite valleys. As a result, their drift velocity begins to decrease until it reaches a steady state value. This final value is dictated by the material parameters and physically represents a dynamic equilibrium between the $\Gamma \rightarrow L$ and $L \rightarrow \Gamma$ valley transitions. The steady state electronic velocities are lower at higher fields, because a larger fraction of electrons occupy the higher mass satellite valleys.

For low fields such as 2 kV/cm and 5 kV/cm, the drift velocity rises more slowly than at the higher field of 10 kV/cm, and the steady state values are correspondingly high. In fact the rise at low fields such as 2 kV/cm is monotonic with no overshoot. The underlying reason is that electrons, at low fields, gain energy very slowly and transfer to the satellite valleys is limited. Such limited satellite valley transfer also accounts for the higher steady state velocity value as compared to the 20 kV/cm case.

All four transient velocity curves of Figure 14 are in excellent agreement with several results available in the literature [28, 43]. This quantitative consistency further demonstrates the successful implementation of the Monte Carlo procedure for the present purposes. Finally, Figure 15 shows the transient electron velocity for a nonuniformly

doped device with concentrations at the left, middle, and right portions of 4 x 10^{16}/cc, 1.0×10^{16}/cc, 4 x 10^{16}/cc, respectively. The device dimensions remained the same as in Figure 10. The transient velocity curve was obtained by using the Poisson solver at a bias of 2 volts. The general shape shows the characteristic overshoot and is typical of device turn-on. A turn-off transient was also simulated by setting the bias to zero after 2.5 psecs. The delay in the turn off is in the picosecond time scale and is controlled by momentum relaxation within the device.

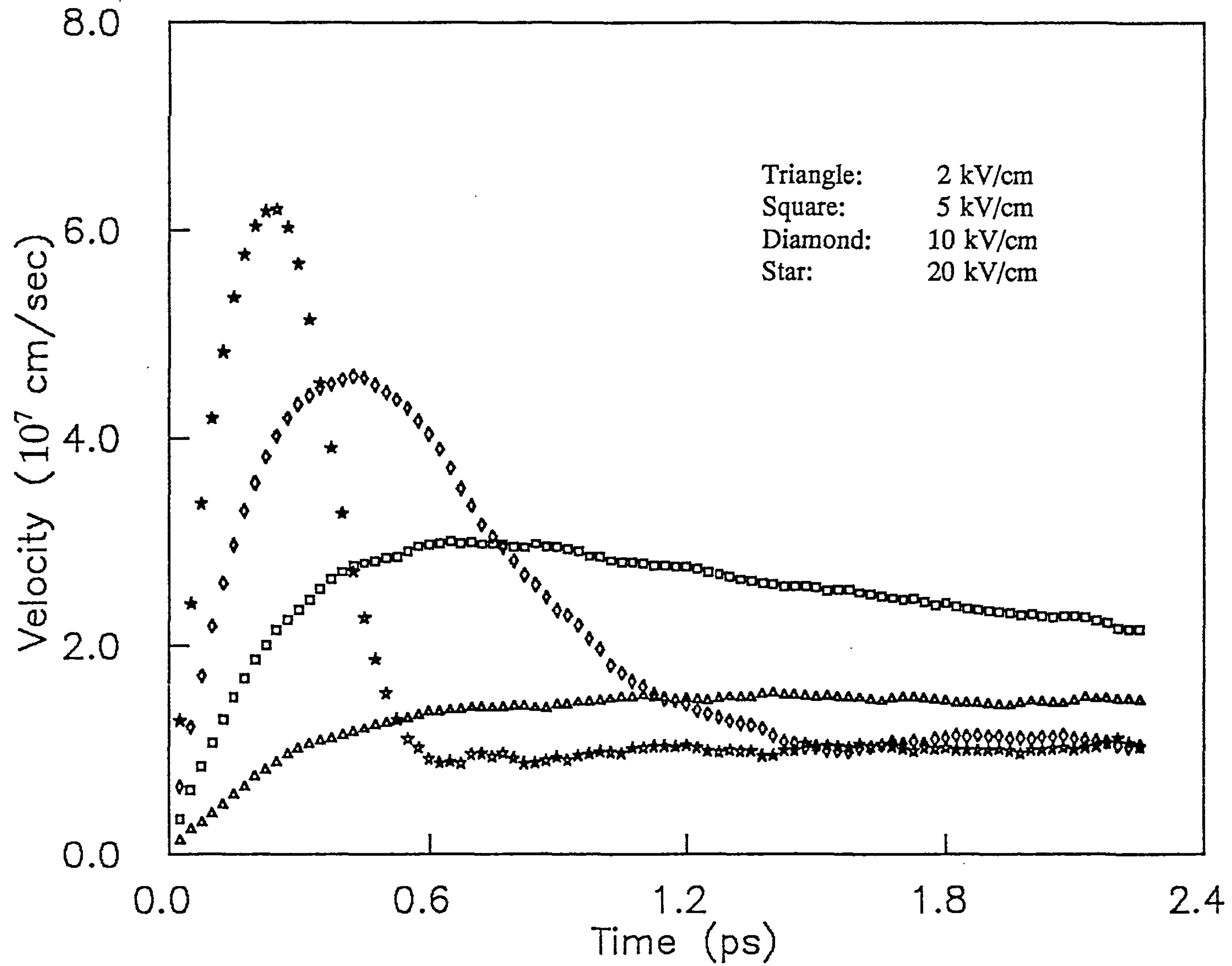

Figure 14. Transient electron velocity curves for different values of electric field.

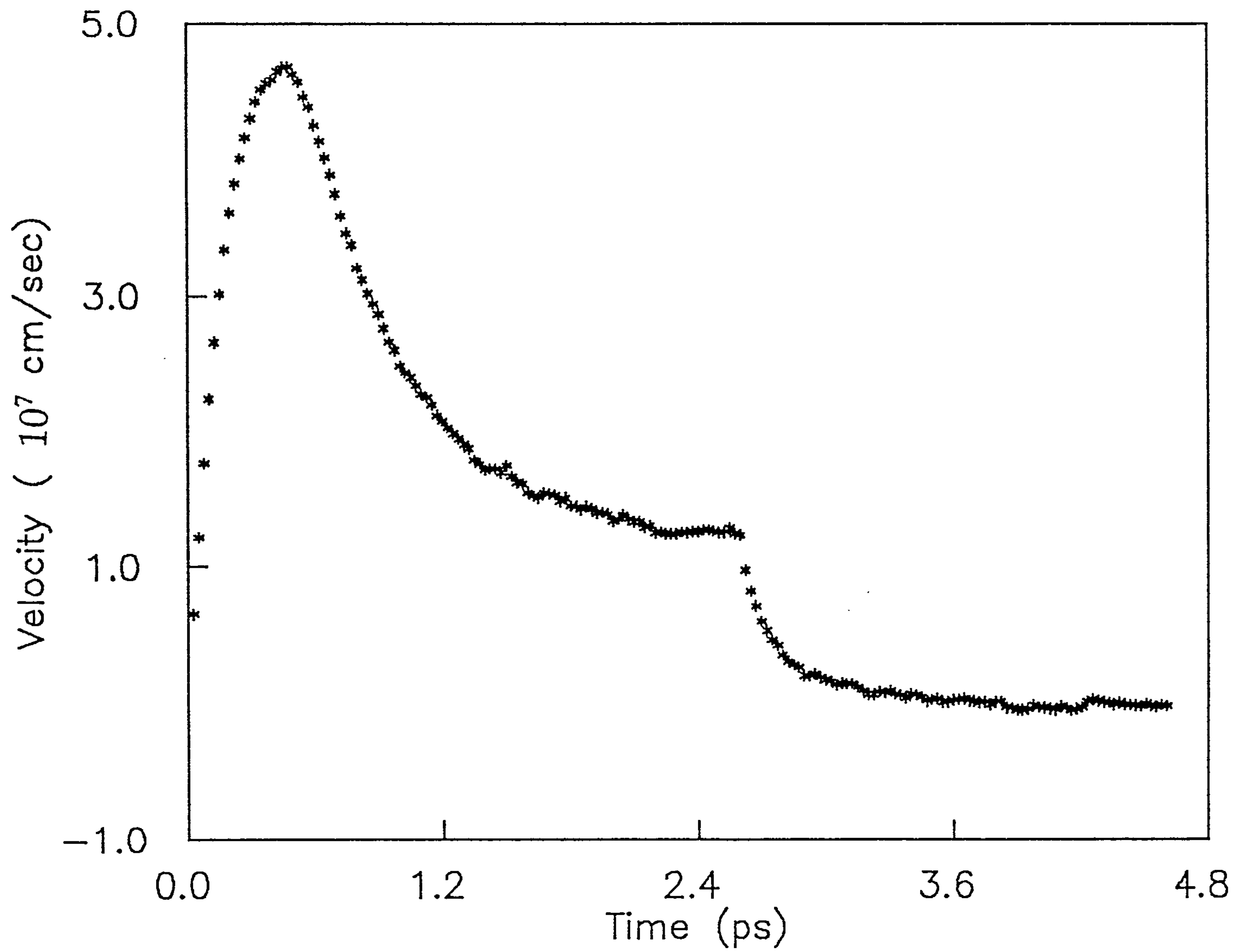

Figure 15. Turn−off transient electron velocity for the electric field of 20 kV/cm within an inhomogeneous structure.

CHAPTER 4

GUNN DIODE AS A RELAXATION OSCILLATOR

This chapter presents an exact large-signal simulation of a millimeter-wave Gunn-effect oscillator. As we have seen in the previous chapter, the simulation properly accounts for all significant relaxation /collision phenomena by utilizing the Monte Carlo technique of Fawcett, Boardman and Swain [30]. The device modeled is of current design with heavily doped contacts; these contacts hence do not require an approximation to force terminal electric fields to zero. The device when coupled with the external circuit oscillates in the fundamental mode at 80 GHz. The interpretation of the device behavior which for the first time is based upon the latest knowledge of electron physics, includes familiar phenomena: electrons are seen to " overshoot " traditional peak velocities, and a " dead zone " at the cathode is found where electrons never gain sufficient energy to transfer to satellite valleys. Computer calculations of the behavior in a resonant circuit of a Gunn diode with bulk negative resistance properties have been made to determine the optimum device and circuit parameters for efficient RF generation. Simulations have also been performed to investigate the performance of both conventional and heterostructure devices. In addition, changes in both the local concentrations and in the alloy composition of the ternary material have been deliberately included to monitor their impact on the

output efficiencies. The following section principally discusses the results of operation for the diode in the Gunn mode [31].

The Gunn mode is defined here as that for which current oscillations take place when the device is biased above its critical voltage in a constant voltage circuit (zero ac impedance). A natural extension of this mode involves the addition of an impedance within the circuit to deliver RF power to the load. The frequency of the Gunn mode in a low impedance circuit is approximately the high-field domain drift velocity V_d divided by the length of the diode L and is primarily determined by L although V_d is somewhat dependent on bias voltage and doping level [32].

4.1 The Device Model

We begin by describing briefly the device model for the conventional Gunn diode structure. The heterojunction device is similar in nature and its model is very similar to the one being discussed here. The only change would be in the material parameters, doping profiles and alloy composition. For the simulation of the conventional Gunn diode, a 50-percent notch in doping near the cathode was included as shown in Figure 10, to provide an initial high field region so that the dead zone could be reduced. The device was divided into 100 spatial cells. The cell size of 0.20×10^{-5} cm was chosen to meet the numerical convergence requirements of Thim [33]. The total number of Monte Carlo electrons used in the simulation was 14,600, with each Monte Carlo electron representing 1.014×10^4 real electrons in a real device. (The number of electrons was limited by the size of the computer memory and reasonable execution time.)

The electric field each electron was subjected to was calculated by first evaluating the internal instantaneous electric field of each cell according to

$$E(n,t) = E(n-1,t) + [MI(N) - MM(N,t)].\frac{q.\Delta x}{\varepsilon} \tag{4.1}$$

where N is the cell number, MI(N) is the number of ions in each cell representing the real doping density, MM(N,t) is the number of electrons in each cell, q is the electronic charge (1.6×10^{-19} C), Δx is the cell size ($.20 \times 10^{-5}$ cm), and ε is the dielectric constant ($12.53 \times 8.854 \times 10^{-14}$ F/cm^2).

Each electron was allowed to drift and suffer collisions for 7.5×10^{-15}s after which external circuit interaction was determined, voltages were updated at the device boundaries and a new electric field was calculated. Electrons which crossed the anode or cathode boundaries during flight were replaced, to satisfy charge neutrality at the cathode or anode, respectively, by electrons randomly chosen from a room temperature Boltzmann distribution. The instantaneous electronic current flowing through the device is given as:

$$I_d(t) = \frac{q\ S}{L} \sum_{i=1}^{N} V_i(t) \tag{4.2}$$

where S is a scale factor relating the number of real electrons per cell to the number of Monte Carlo electrons ($S = 1.014 \times 10^4$ as given earlier). N is the total number of Monte Carlo electrons, $V_i(t)$ is the velocity of the ith electron at a given time 't' and L is the length of the device. This electronic current was used in the calculations presented below for the device circuit interaction.

4.2 Numerical Simulations

The Gunn oscillator circuit chosen to support the microwave oscillation is shown in Figure 16. It is a parallel resonant circuit with a capacitance composed of the device dielectric capacitance C_D and an external capacitance C_L in parallel with a load resistance, and the equivalent combination is in series with an inductance. The battery voltage is applied in series with the inductance. The external capacitance was chosen to equal three times the device capacitance, by trial and error, to achieve good oscillations.

The time dependent current $I_t(x,t)$ at a generic position in the device is given by

$$I_t(x,t) = I_e(x,t) + \epsilon A \frac{\partial E(x,t)}{\partial t} \tag{4.3}$$

where $I_c(x,t)$ represents the particle current and $\varepsilon A \partial E(x,t)/\partial t$ the displacement current. A is the cross-sectional area of the device, and ε is the dielectric constant. Since the total current is constant throughout the device at any given time, one can integrate the above equation over the device length W as :

$$I_t(t) = \frac{1}{W}\int_0^W I_e(x,t)dx + \frac{\epsilon A}{W}\frac{\partial V}{\partial t} = I_d(t) + C_{cold}\frac{\partial V}{\partial t} \tag{4.4}$$

where V is the instantaneous potential across the device. The quantity $\epsilon A/W$ referred to in the above equation is usually called the cold capacitance [34].

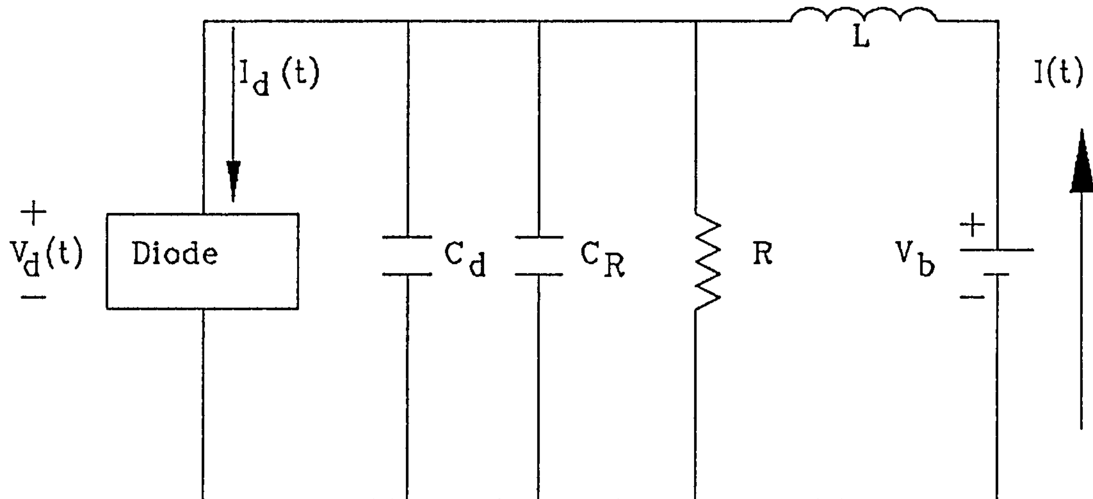

Figure 16. Schematic diagram of the parallel resonant circuit used for the simulation of a Gunn diode oscillator

The tank circuit in Figure 16 is simulated using Kirchoff's circuit equations

$$V_D(t) = V_B - L\frac{dI(t)}{dt} \tag{4.5}$$

$$I(t) = I_d(t) + C\frac{dV_D(t)}{dt} + \frac{V_D(t)}{R} \tag{4.6}$$

where $V_D(t)$ is the instantaneous voltage applied to the device terminals, V_B is the dc bias voltage, I(t) is the instantaneous current flowing through the battery, and C is the total capacitance (parallel of the circuit and the cold capacitance).

Equations (4.5) and (4.6) are discretized using finite differences in time and they are written as:

$$I(t + \Delta t) = [V_B - V_D(t)]\frac{\Delta t}{L} + I(t) \tag{4.7}$$

$$V_D(t + \Delta t) = [I(t) - I_d(t)]\frac{\Delta t}{C} + V_D(t)[1 - \frac{\Delta t}{RC}] \tag{4.8}$$

In the present analysis, the particle current $I_d(t)$ was computed at each time step within the EMC algorithm. A three valley nonparabolic model was used to simulate the electronic motion based on the effective mass approximation. All the relevant scattering mechanisms such as polar optical, acoustic deformation potential, equivalent- and nonequivalent intervalley phonon, and ionized impurity scattering were comprehensively included. The Poisson solver was used at the end of each time step to update the internal electric field in response to electronic motion. A three point centered difference scheme was used to discretize Poisson's equation. Finally, two device structures were chosen for

the current simulation purposes. One was a conventional notch oscillator described in the previous section while the other structure incorporated a heterojunction. The simulated device structure for $Al_{0.3}Ga_{0.7}As$-GaAs-GaAs heterojunction cathode oscillator is shown in Figure 17. The conventional device served a dual purpose, first as a standard accuracy check for the proposed EMC scheme and secondly, as a basis for comparison against the more advanced heterostructures. Both of the simulated devices had a uniform doping level of 10^{16} cm^{-3} in the central drift region. The two n-type contacts were assumed to be equally doped with densities of 4 x 10^{16} cm^{-3} over a distance of 0.16 μm. The total device length was chosen to be 2.0 μm, with an area of 5 x 10^{-5} cm^{-2}. For the notch structure the doping density adjacent to the cathode was reduced to a value of 5 x 10^{15} cm^{-3} over a distance of 0.08 μm to create the high field region. As is well known, such a local field profile works to reduce the dead zone, initiate charge instabilities and to transfer electrons into the satellite valleys. The heterostructure oscillator, on the other hand, does not require a notch since the bandgap difference automatically sets up a local electric field nonuniformity. The material composition for the heterostructure as shown in Figure 17 leads to a band offset of 0.22 eV. Typical circuit parameters were used for the simulation and included a 23.44 Ω resistor, a 3.66 pH inductance, and a 1.08 pF capacitance. Based on these values, the natural frequency of the RLC network works out to be 80 GHz. This frequency was chosen since it is near the atmospheric attenuation window for telecommunication applications. In order to monitor the temporal changes and accurately update the current/voltage values, a time interval much shorter than the natural time

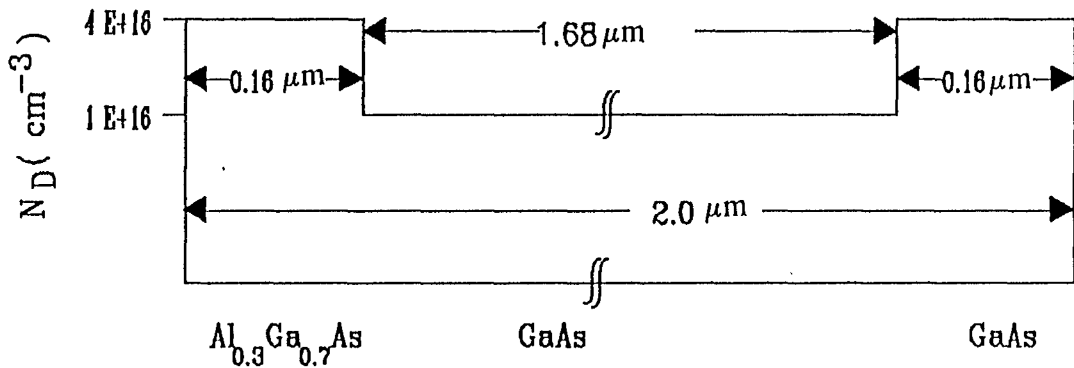

(a)

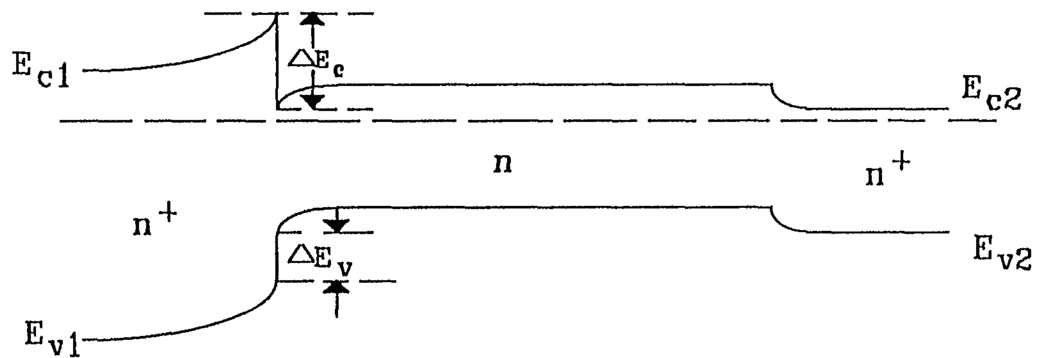

(b)

Figure 17. Heterostructure oscillator a) the doping profile for the simulated $Al_{0.3}Ga_{0.7}As$–GaAs–GaAs structure, and b) equilibrium energy band diagram.

period has to be used. Convergence towards steady state repetitive waveforms in the present case was generally obtained after about four or five cycles.

The details of the electron transport inside the conventional notch oscillator are discussed below. In Figures 18 and 19, we plot the distribution of electrons in the Γ, and L valleys to show the amount of intervalley transfer, which is the essential ingredient of the Gunn effect. From these Figures, one can see that about half of the active region is required to accelerate a substantial concentration of electrons to the threshold energy for intervalley transfer. Furthermore, it is explicitly seen that the electrons which are in front of the domain are in the slower satellite valleys, while the electrons behind the accumulation layer are in the faster Γ valley. Consequently, the electrons tend to pile up, thereby increasing the size of the accumulation layer as seen from Figure 19. In order to demonstrate that the dead zone has been reduced in the heterostructure device as shown in Figure 17, we plot Figures 20a and b comparing the distribution of electrons in both devices at the time instant 3T/4. It is obvious from Figure 20b that the electron accumulation in the L valley exceeds the electron population in the Γ valley at a distance of 0.85 μm from the cathode for the heterostructure oscillator. For the conventional notch oscillator on the other hand, a distance of 1.05 μm from the cathode is required as shown in Figure 20a. This effectively proves that the dead zone is indeed reduced by using heterostructures. The physical mechanism responsible for this effect is the conduction band offset energy at the junction of AlGaAs/GaAs interface which provides a high field region, enabling electrons to gain higher energies and hence intervalley transfer nearer the cathode.

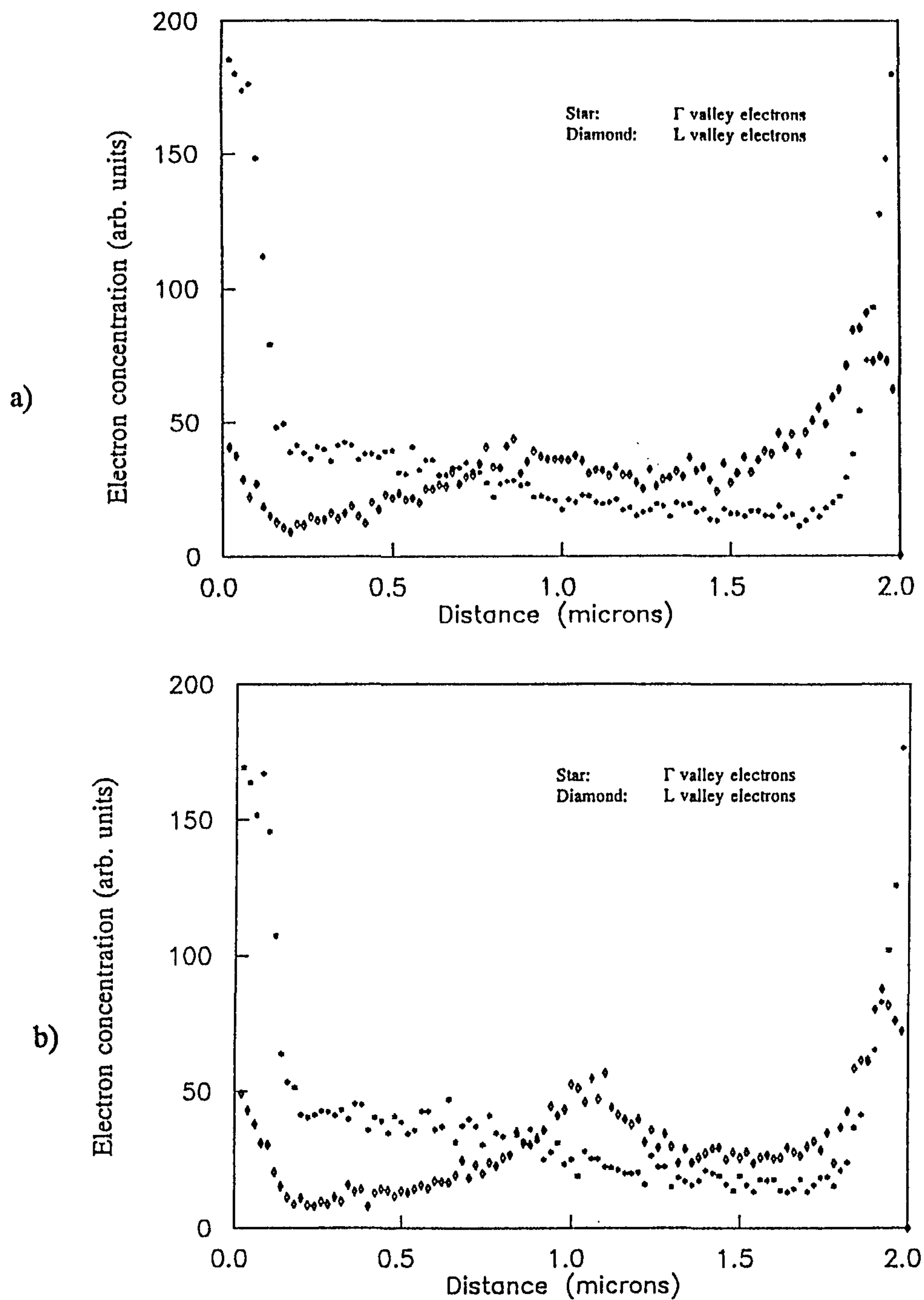

Figure 18. Valley occupation showing electronic concentration in the Γ and L valleys for the conventional notch oscillator for a bias of 2.0 volts a) at the time instant T/4, b) at the time instant T/2.

a)

b)

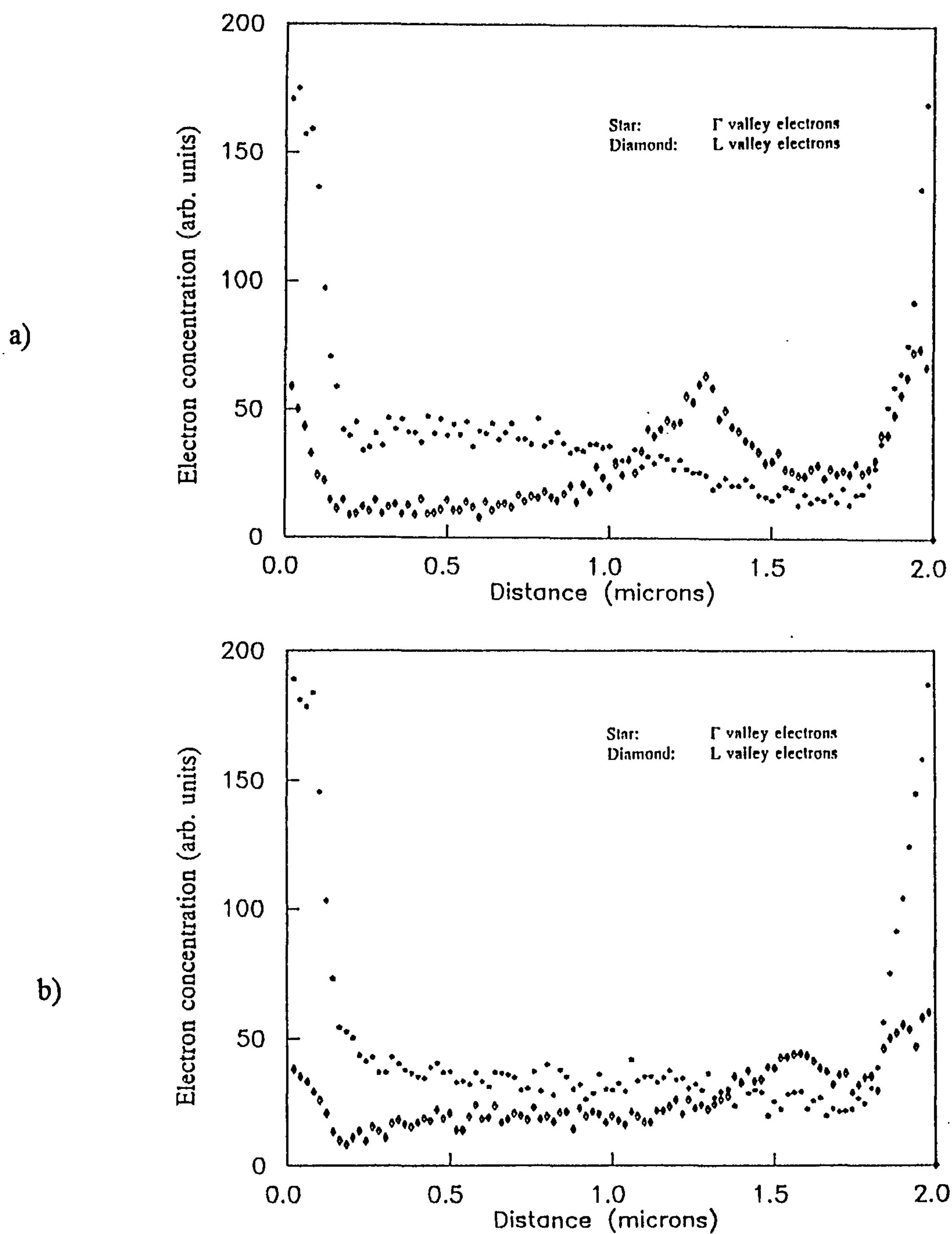

Figure 19. Valley occupation showing electronic concentration in the Γ and L valleys for the conventional notch oscillator for a bias of 2.0 volts a) at the time instant 3T/4, b) at the time instant T.

a)

b)

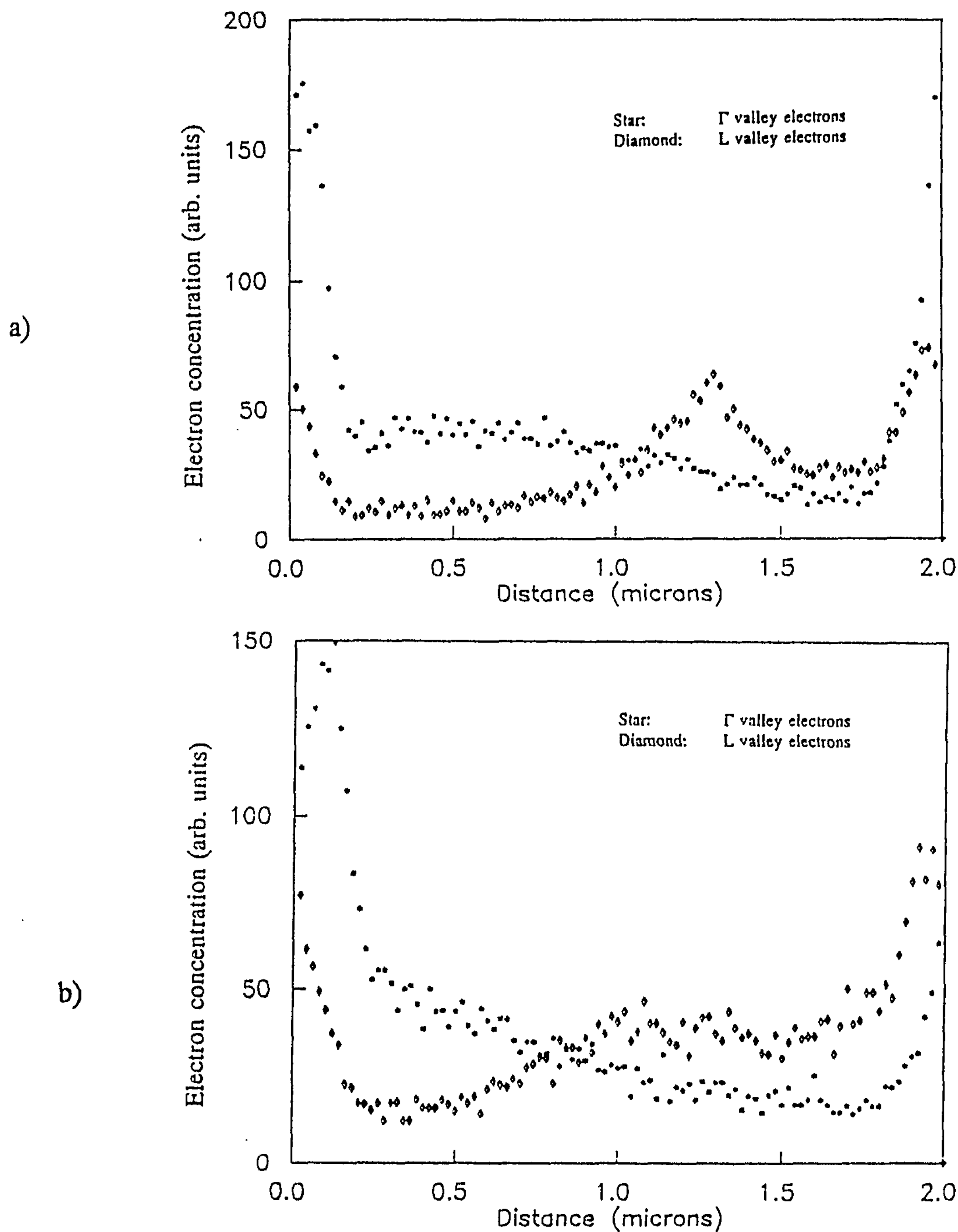

Figure 20. Comparison of electron population in Γ and L valleys at the time instant 3T/4, at a bias of 2.0 volts for the devices a) notch oscillator and b) heterostructure oscillator.

4.3 Discussion of Results

Computer simulations were made for two different chosen device structures for the current purposes. These have been shown in Figures 10 & 17 corresponding to the conventional notch oscillator and a heterojunction configuration respectively. The notch structure was included in the analysis because it serves as a standard accuracy check of the current EMC simulations, and allows relative comparisons to be made with the heterostructure oscillator. Time dependent voltage and current waveforms obtained for the notch oscillator at a DC bias of 3.0 volts are shown in Figures 21-23. The voltage in Figure 21 is across the Gunn diode element, and lags the diode current waveform of Figure 23. Furthermore it is always above the critical threshold required for intervalley transfer. It may also be noted that the diode current is slightly asymmetric and contains harmonic components. This is to be expected given the nonlinear response function of the semiconductor Gunn diode structure. All three waveforms are in very good agreement with previous Monte Carlo simulations [14] and demonstrate a successful implementation of the present numerical scheme. Other simulation with the notch structure were also carried out for a range of bias values to obtain the voltage dependence of the device efficiency, power output, and operating frequency. A comparative study of these parameters against those of the heterostructure device is expected to be very useful.

The curves obtained for the heterostructure at an applied DC bias of 2.0 volts are shown in Figures 24-26. Understandably, the average value of the diode voltage is lower in this case than that of Figure 21 because of the lower applied bias. The general qualitative features, however remain almost the same as before. The main change brought

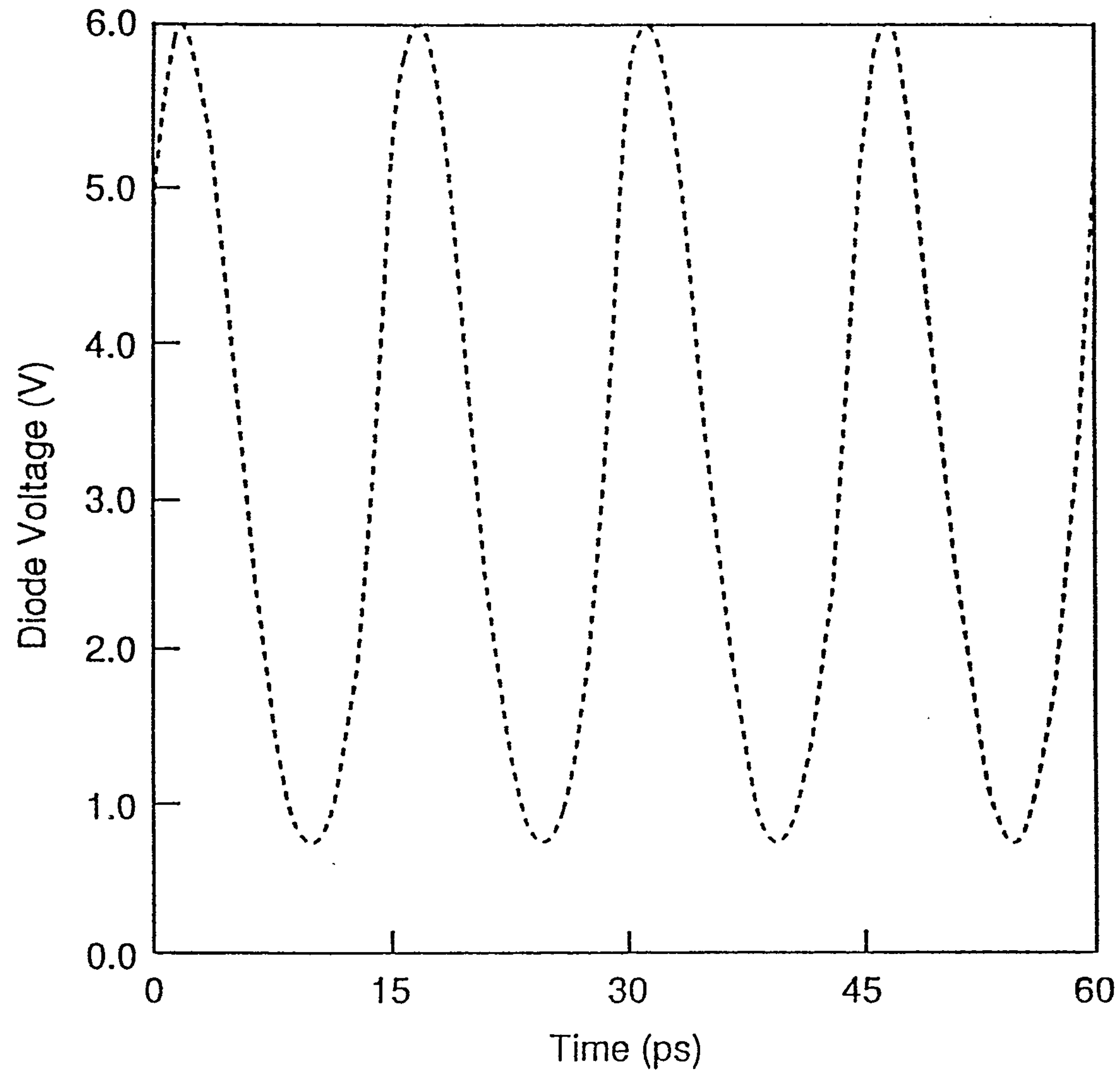

Figure 21. Diode voltage waveform of a notch-type Gunn oscillator at a bias of 3.0 volts.

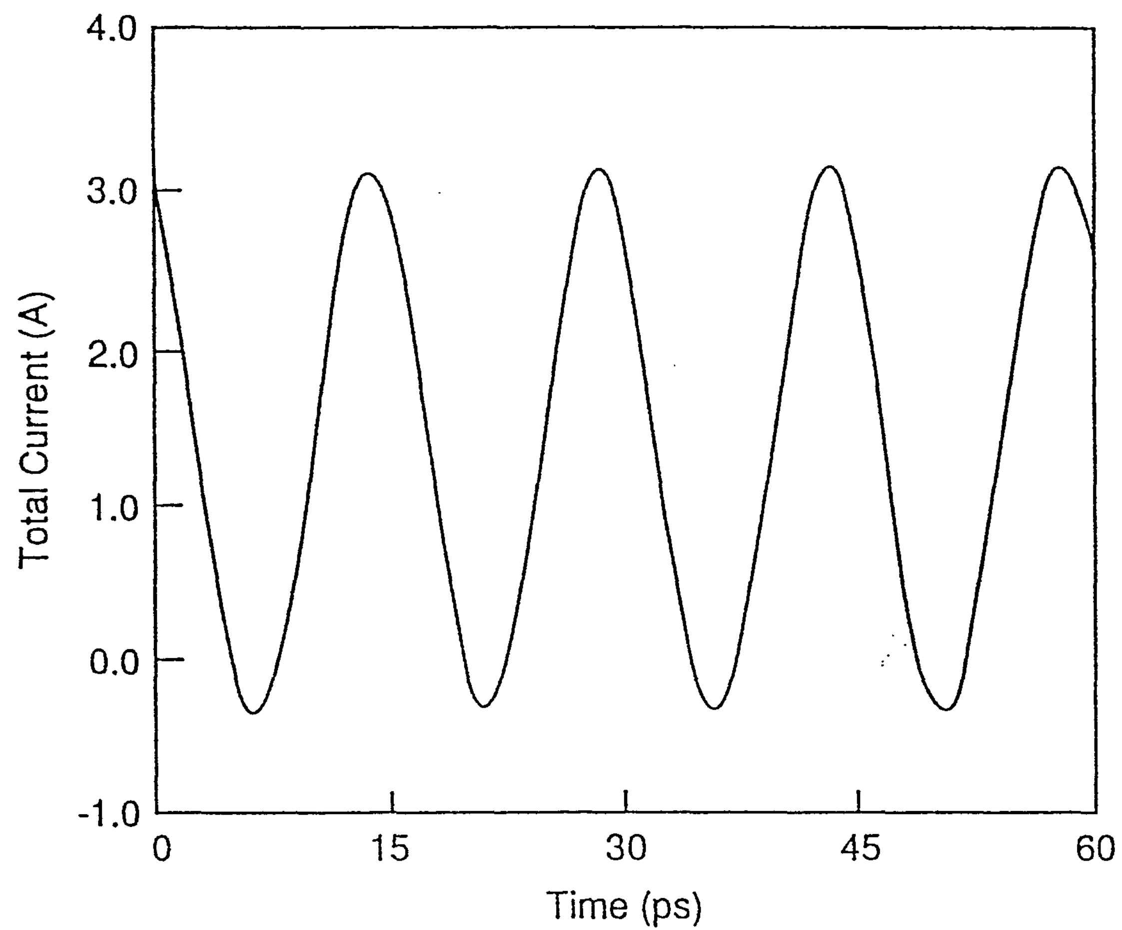

Figure 22. Total circuit current waveform for the notch-type Gunn oscillator at a bias of 3.0 volts.

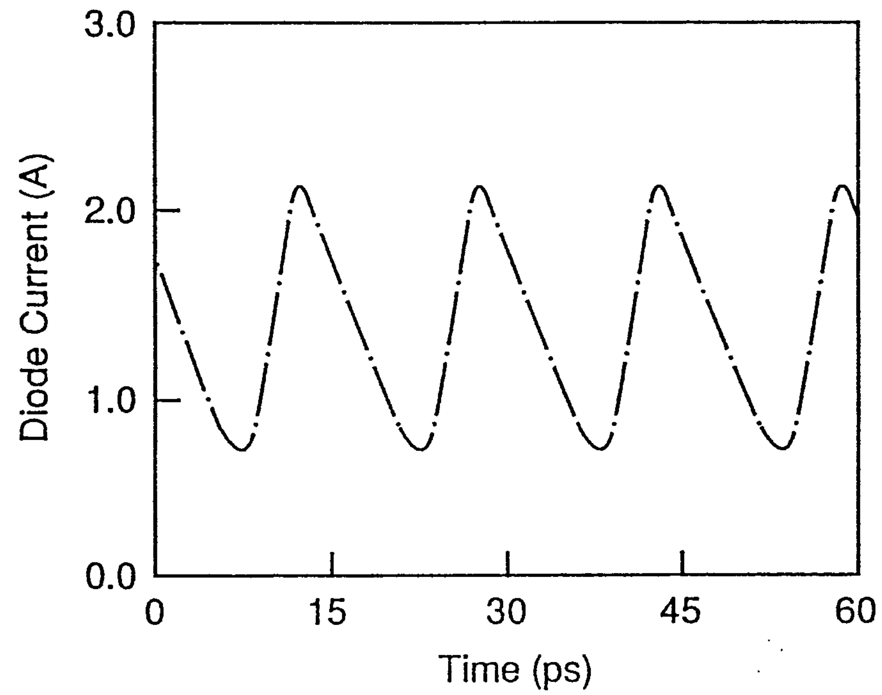

Figure 23. Diode current waveform of a notch-type Gunn oscillator at a bias of 3.0 volts.

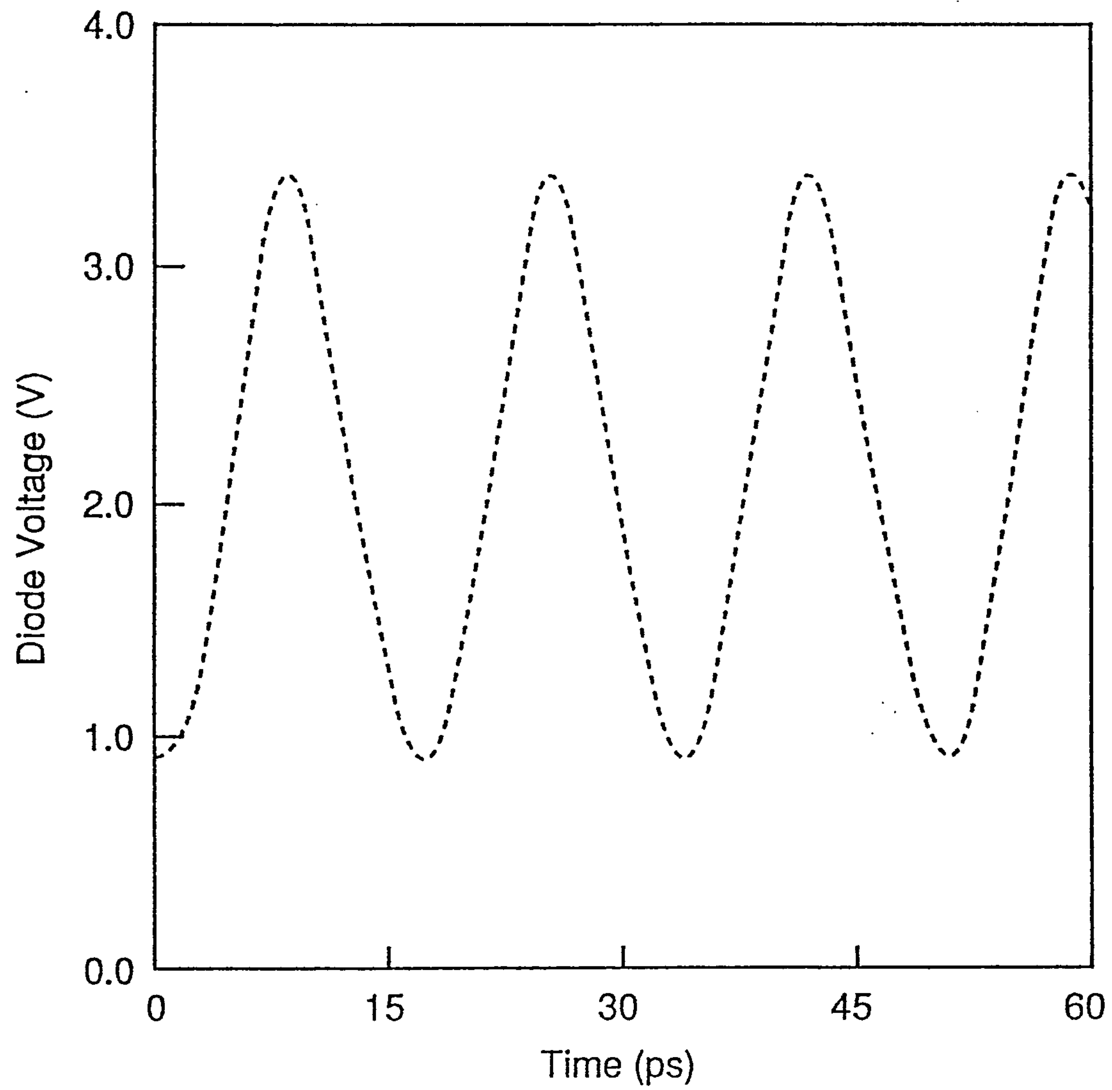

Figure 24. Diode voltage waveform of a heterostructure oscillator at a bias of 2.0 volts.

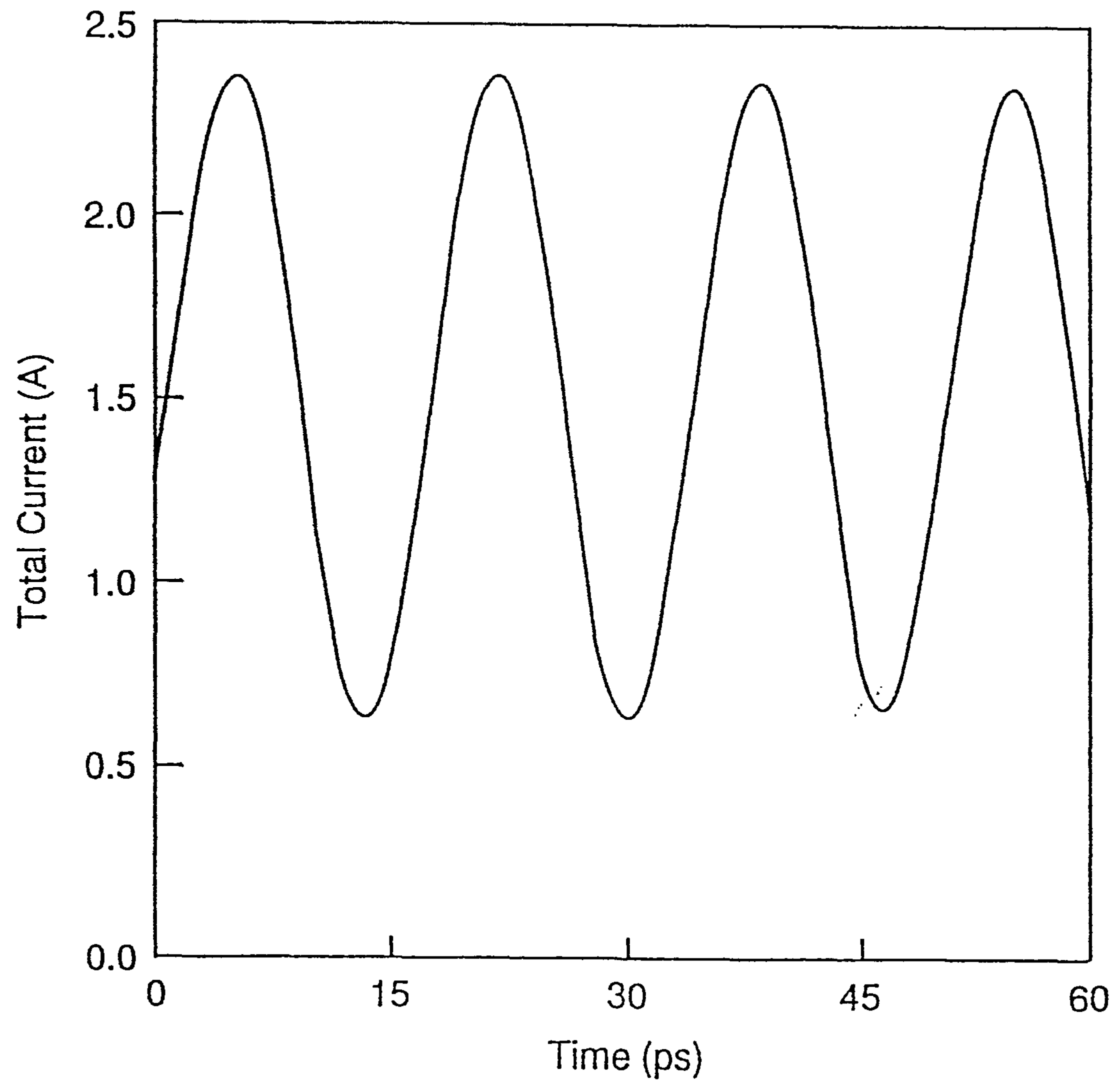

Figure 25. Total circuit current waveform for the heterostructure oscillator with an aluminum composition coefficient of 0.3 at a bias of 2.0 volts.

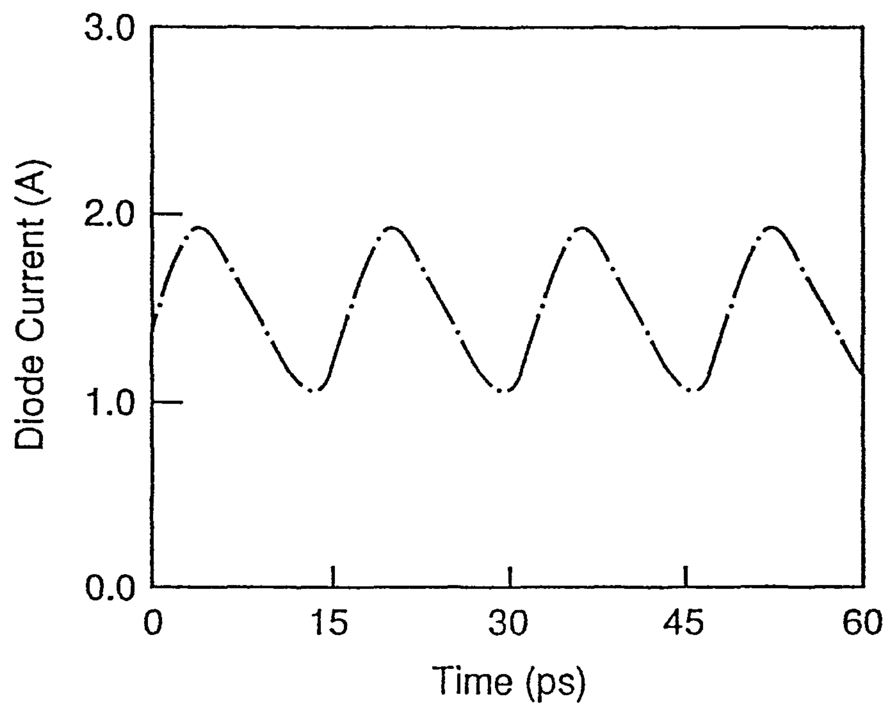

Figure 26. Diode current waveform of a heterostructure oscillator at a bias of 2.0 volts.

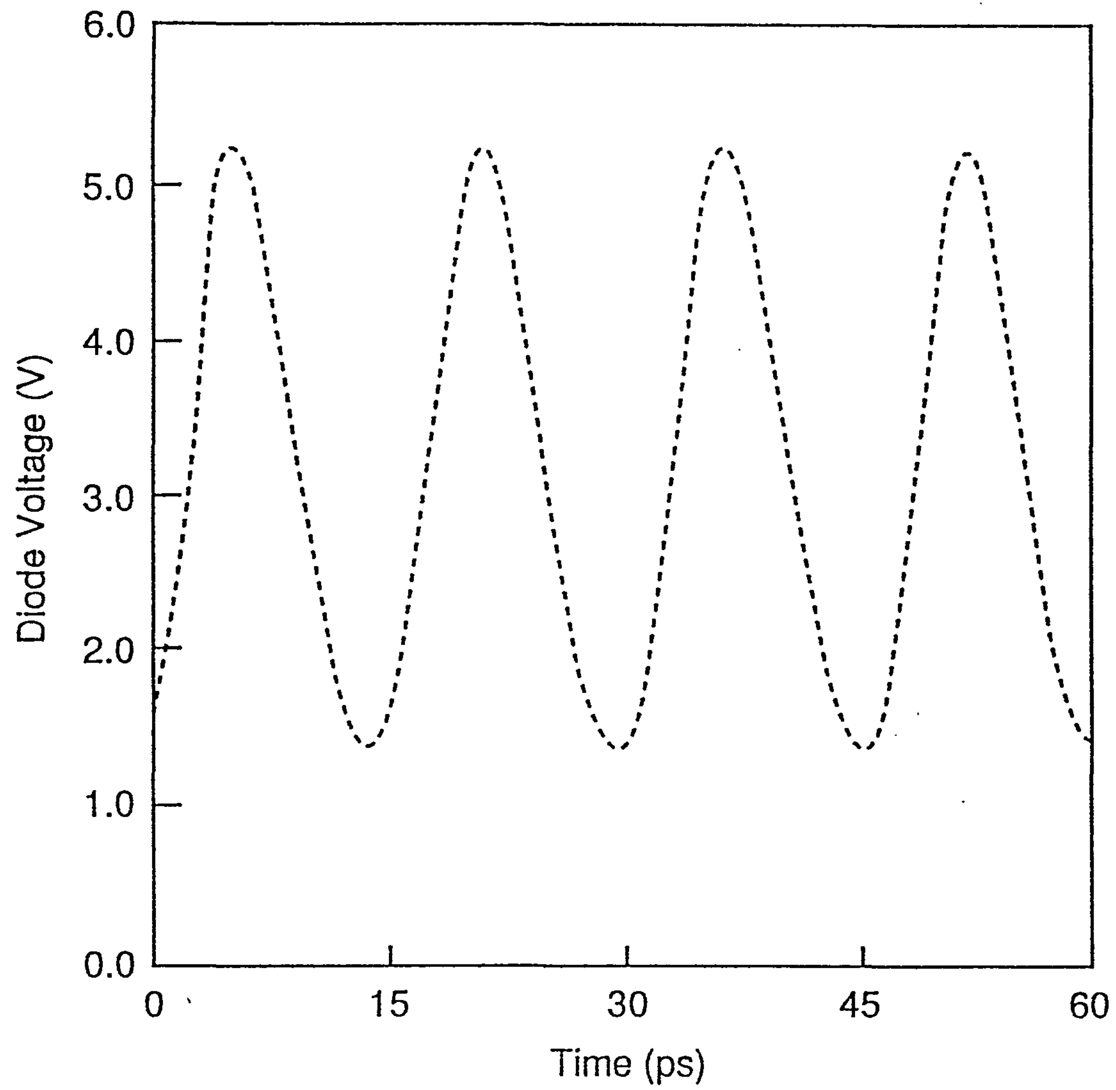

Figure 27. Diode voltage waveform of a heterostructure oscillator with an aluminium composition coefficient of 0.30 at a bias of 3.0 volts.

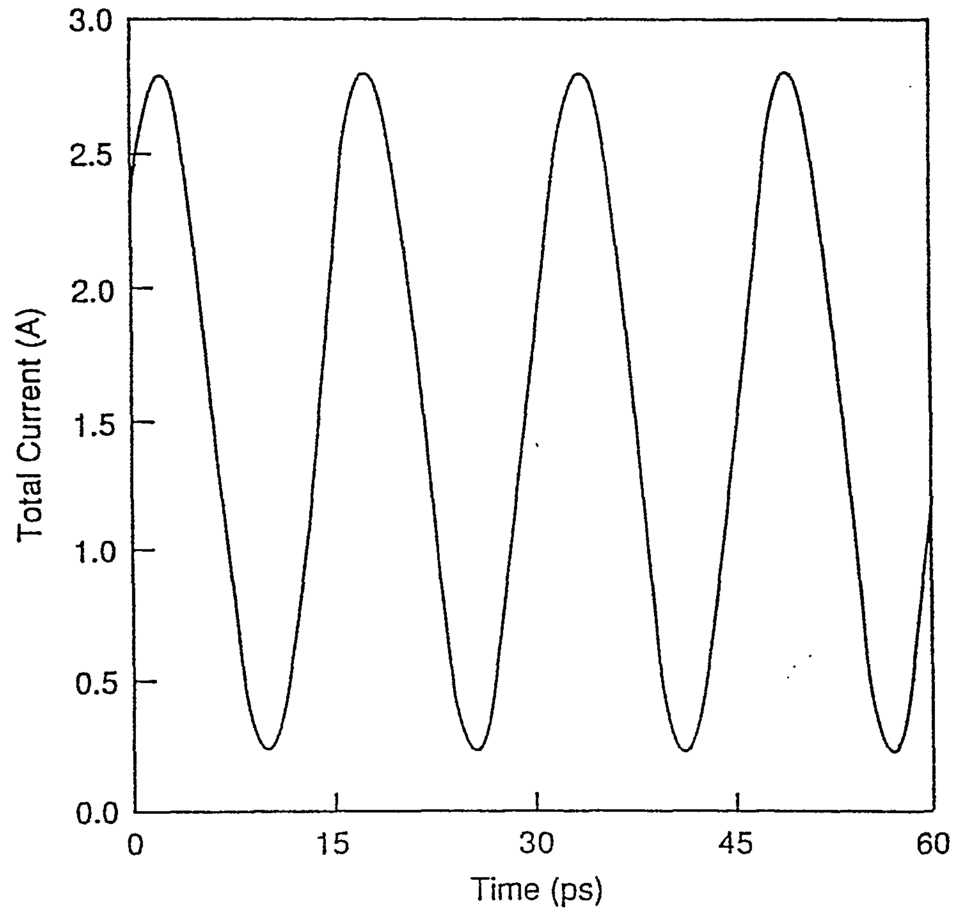

Figure 28. Total circuit current waveform for the heterostructure oscillator with an aluminum composition coefficient of 0.3 at a bias of 3.0 volts.

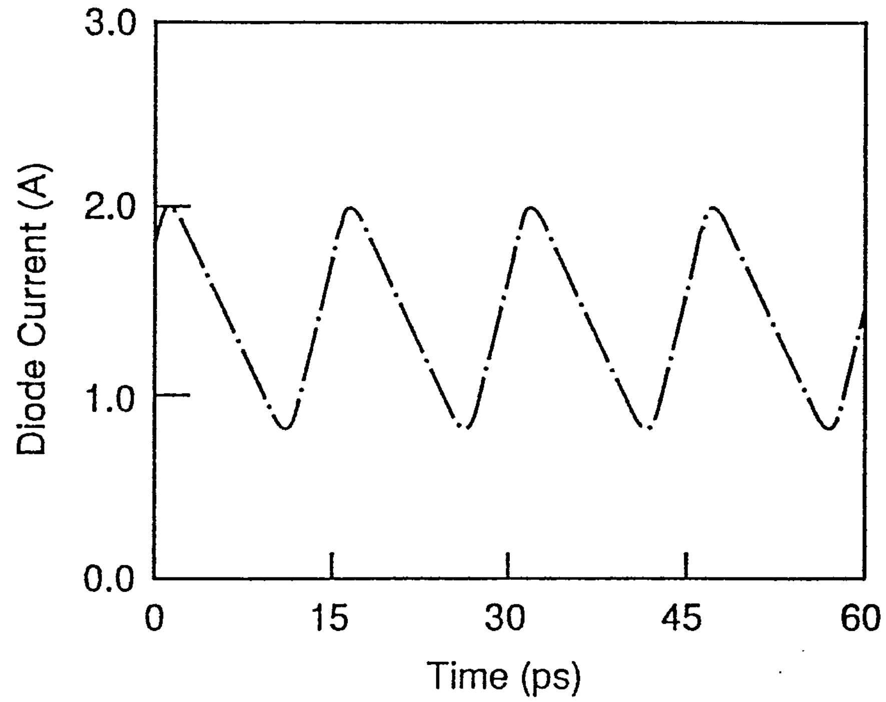

Figure 29. Diode current waveform of a heterostructure oscillator with an aluminium composition coefficient of 0.30 at a bias of 3.0 volts.

about by this configuration is in the effective time period. Besides, as will be shown later, the efficiency and power output are also different. Voltage and current waveforms for the heterostructure diode at a bias of 3.0 volts are shown in Figures 27-29. As expected the voltage across the diode in Figure 27 is much higher than that of Figure 24 with a more pronounced swing. On the other hand, the diode current magnitudes at the voltages of 2.0 and 3.0, neither increase appreciably nor exhibit any significant scaling because of the strong non-linearity inherent in the velocity-field curve. Finally a comparison between the curves of Figure 21 and 27 reveals that the average value of the diode voltage tends to be higher in the heterostructure which in some sense, implies a higher conductivity level. Physically, this can be understood in terms of the distribution of the valley-dependent effective mass population within the two devices. The notch structure relies of a strong carrier heating effect to transfer electrons into the satellite valleys. Hence, of the electrons left behind in the Γ valley, those in the notch structure have relatively higher energies on the average. These relatively higher energies mean greater phonon related scattering and thus leads to a lower effective mobility contribution. Concomitant with this effect would be a reduction in the device operating frequency. This, as will be shown subsequently, does occur and can be explained in terms of the average voltage drops in the circuit. Since, the average diode conductivity is relatively higher for the heterostructure , the total circuit current is higher. This is confirmed by a comparison of Figures 22 and 28. Also, the higher diode voltage of Figure 21 implies that the potential across the inductance has to be lower to satisfy the voltage law across the loop. For a given inductance value then, this lowered inductive voltage translates into a lower operating frequency.

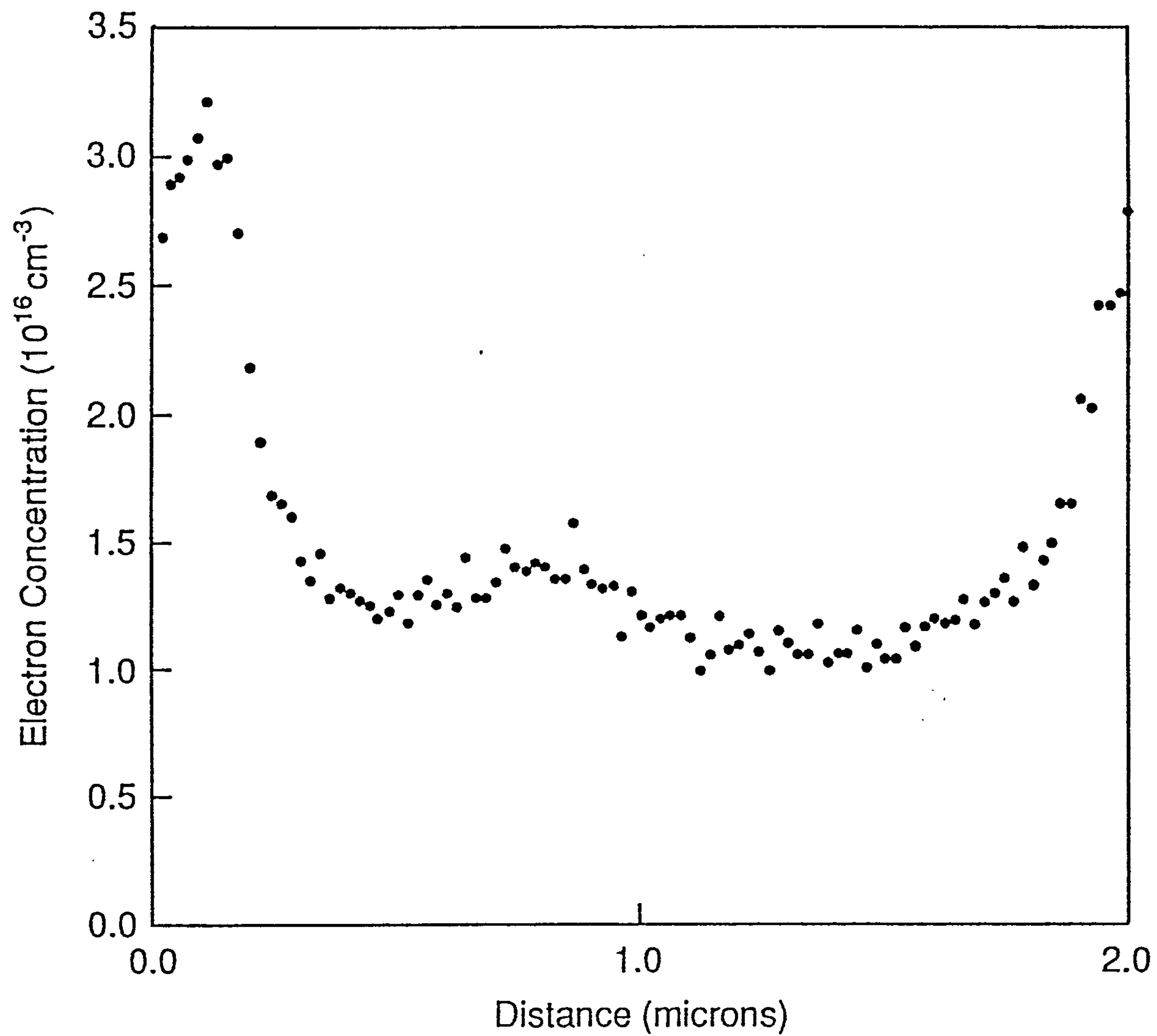

Figure 30. Snapshot picture of the spatial electronic distribution within the heterostructure Gunn diode at a bias of 3.0 volts at the time instant T/4 (one-quarter cycle).

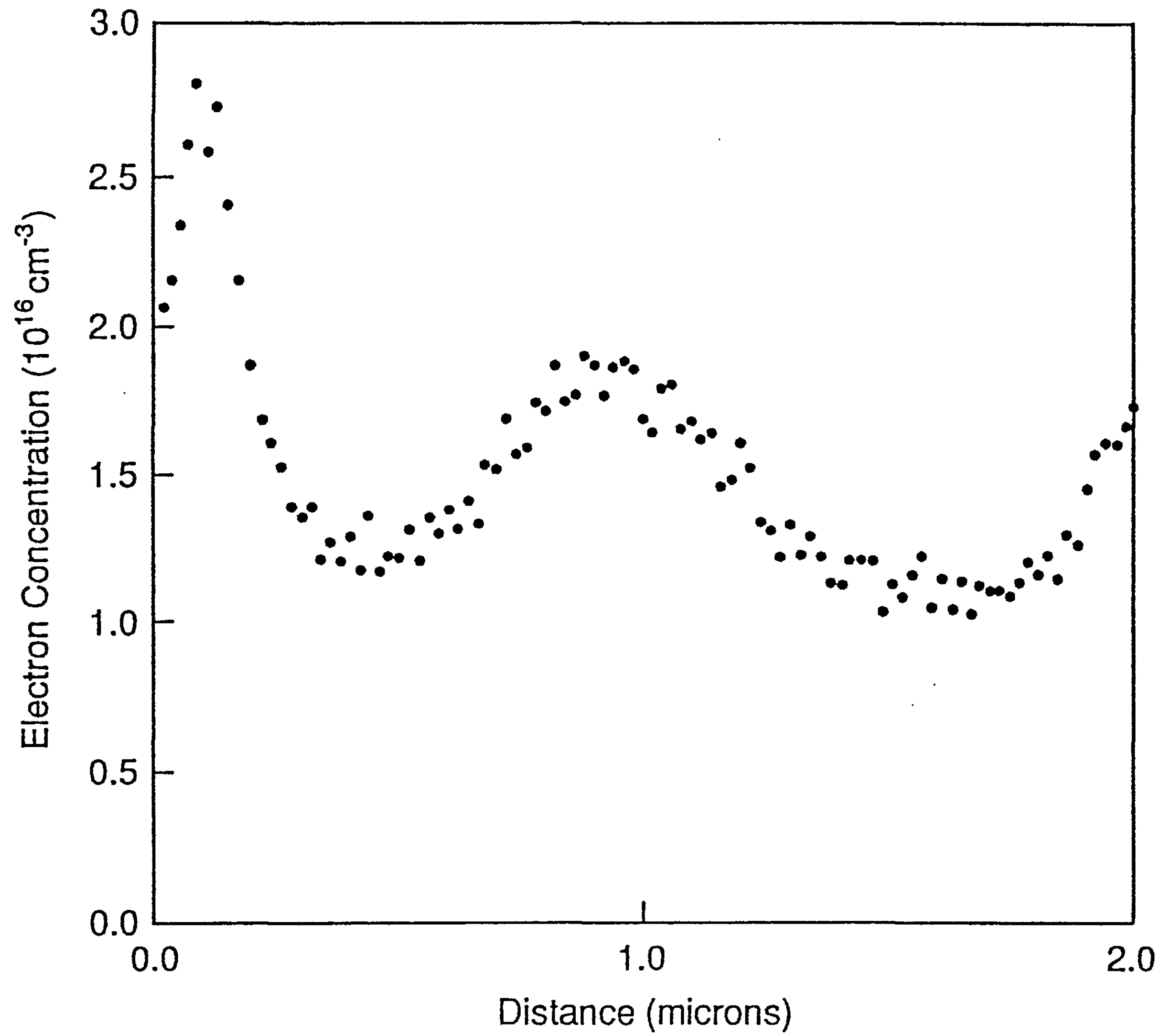

Figure 31. Snapshot picture of the spatial electronic distribution within the heterostructure Gunn diode at a bias of 3.0 volts at the time instant T/2 (one-half cycle).

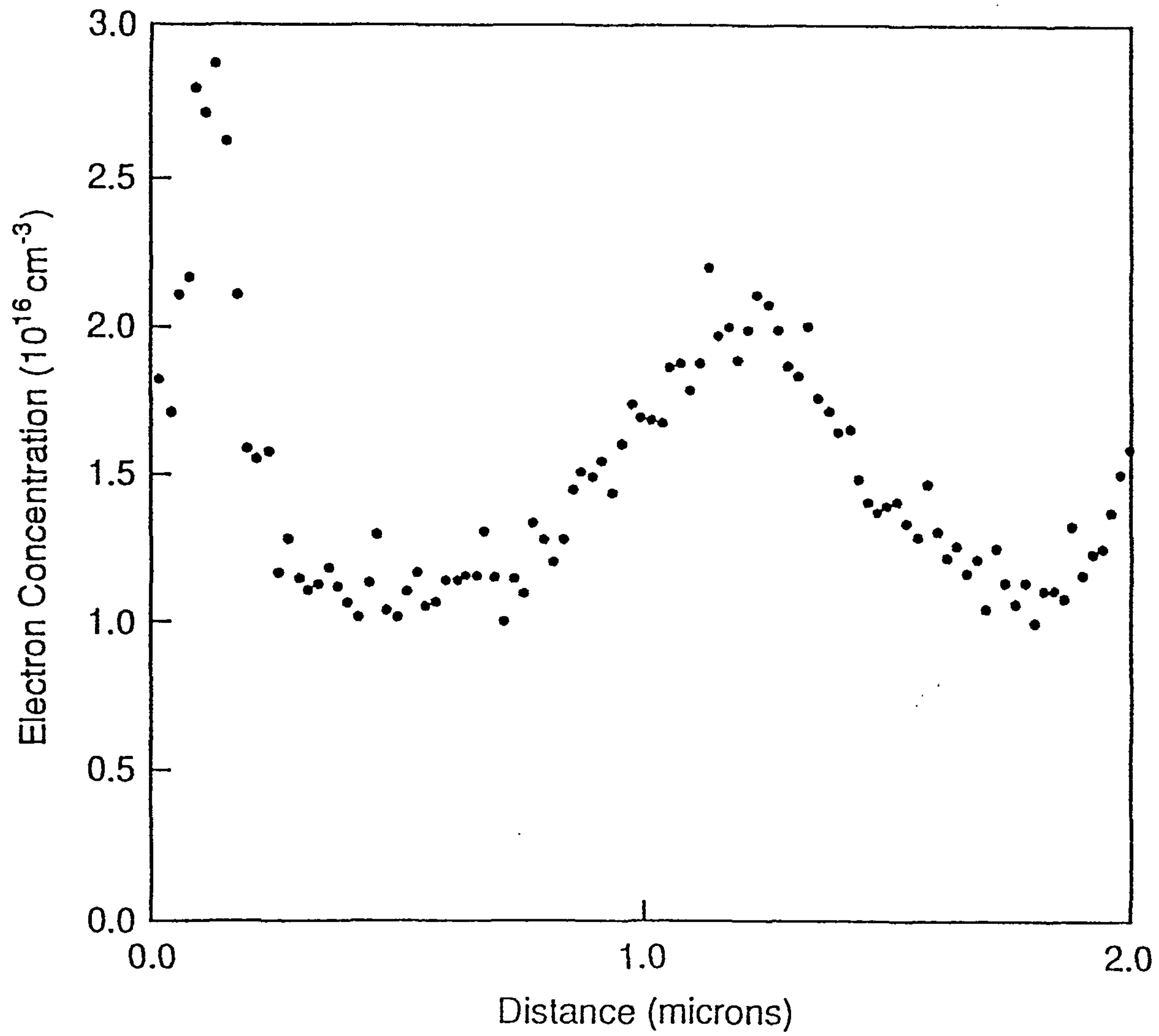

Figure 32. Snapshot picture of the spatial electronic distribution within the heterostructure Gunn diode at a bias of 3.0 volts at the time instant 3T/4 (three-quarter cycle).

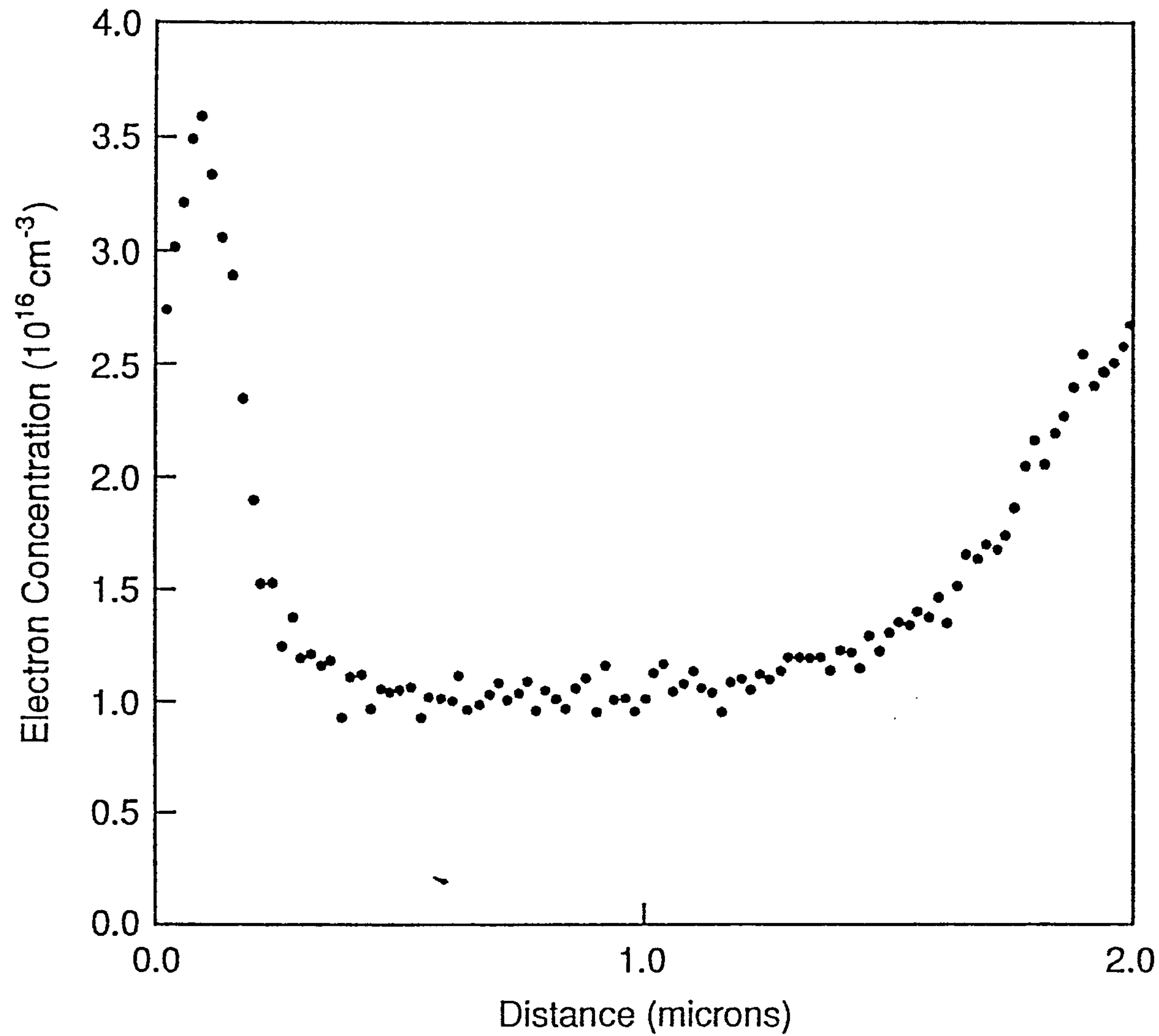

Figure 33. Snapshot picture of the spatial electronic distribution within the heterostructure Gunn diode at a bias of 3.0 volts at the time instant T (one-full cycle).

The periodic movement of the charge carriers across the device over a complete cycle is shown in Figures 30-33. Snapshot pictures of the electronic concentration obtained from the Monte Carlo are indicated for the time instants t= T/4, t=T/2, t=3T/4, and t=T. During transit, electrons move towards the right. As can be seen from a comparison of Figures 30 and 31, the movement during the latter part of the cycle is much slower. This is because a greater fraction of the electrons reside within the low mobility satellite valley. Furthermore some initial time is required to build up the charge instability as apparent from the Figures 32 and 33.

A scheme suggested for improved Gunn diode performance is based on the injection of hot electrons into GaAs using graded $Al_xGa_{1-x}As$ structures [35]. The energy of injection of the hot electrons is equal to the conduction band offset between the $Al_xGa_{1-x}As$ and GaAs at the heterojunction formed between the two materials, and is typically between 200 and 300 meV. A variety of such hot-electron injectors have been reported [36] - [41]. The present study focussed on the use of such compositionally graded AlGaAs layers, to exploit the increase in the bandgap with enhancements in the alloy composition. From the observation that the conduction band offset energies in this material system can be chosen to be nearly equal to the Γ-L valley separation (330 meV), we anticipated a modification to the intervalley scattering statistics in the immediate vicinity of a AlGaAs/GaAs junction. Schematic diagram of our injector structure is shown Figure 34. In this simplest design, we have linearly graded $Al_xGa_{1-x}As$ layer, where x increases from 0 to 0.2 over 160 nm, against the transit region. This structure would give an injection energy of some 250 meV, close enough to the Γ - L valley energy separation

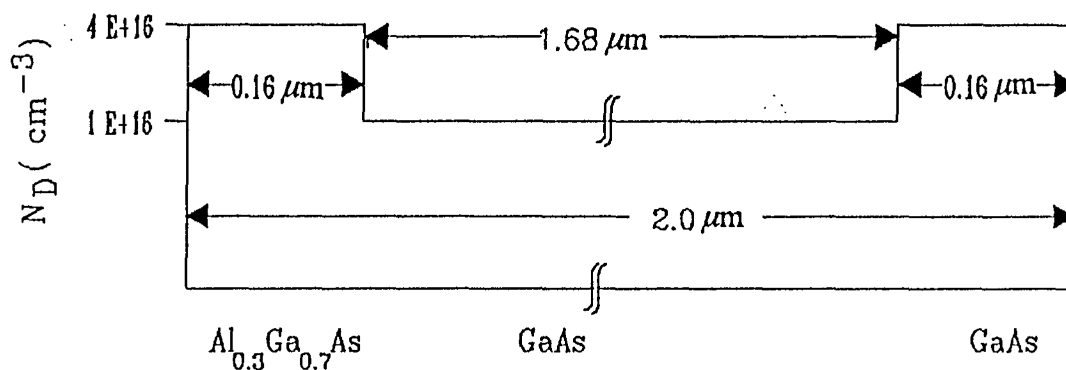

(a)

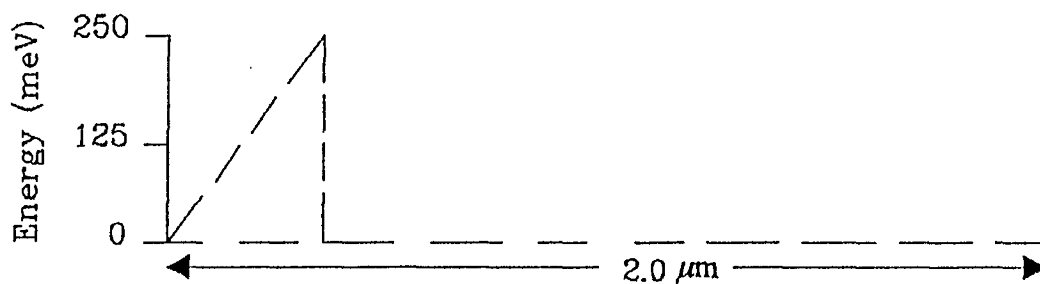

(b)

Figure 34. The simulated structure for $Al_{0.3}Ga_{0.7}As$–GaAs–GaAs oscillator with a graded injector at the cathode.
(a) the doping profile, (b) the energy of the point of the conduction band, through the device.

for significant electron transfer. The solid lines show the doping profile, and the dashed line represents the energy of the Γ point of the conduction band through the device. Monte Carlo calculations were done at a bias of 2.0 and 3.0 volts. We obtained an ac power output of 777 mW in the frequency range of 60 to 65 GHz. The efficiency of the heterostructure is seen to be smaller than the notch device at the low voltage levels. A comparison of the ac power delivered, on the other hand appears to be more favorable. With increasing bias, the heterostructure efficiency improves considerably and is slightly better than that of the conventional device. Consequently applications requiring relatively higher power outputs might operate better with heterostructure Gunn diode configurations. It has to be pointed out, however that quantum mechanical tunneling was not included in the simulations. This process, if modelled would have an additive contribution in this configuration.

As suggested by Ondria and Ross [24] and Beall et al [42], the doping profile in the transit region of a conventional Gunn diode could be graded to improve the diode performance. This can be explained briefly as follows. The microwave power obtainable from Gunn oscillators is limited by device heating produced by the nonuniform dielectric field within bulk GaAs. Hence, both the power and the efficiency can be improved by removing any of the heating effects and tailoring the electric field towards more uniform profiles. An attractive possibility is to vary the doping profile in the transit region in a logarithmic fashion, from a high value at the cathode to lower concentration at the anode. A greater uniformity in the electric field throughout the transit region can thus be achieved when the device is in operation. To numerically evaluate this, simulations were

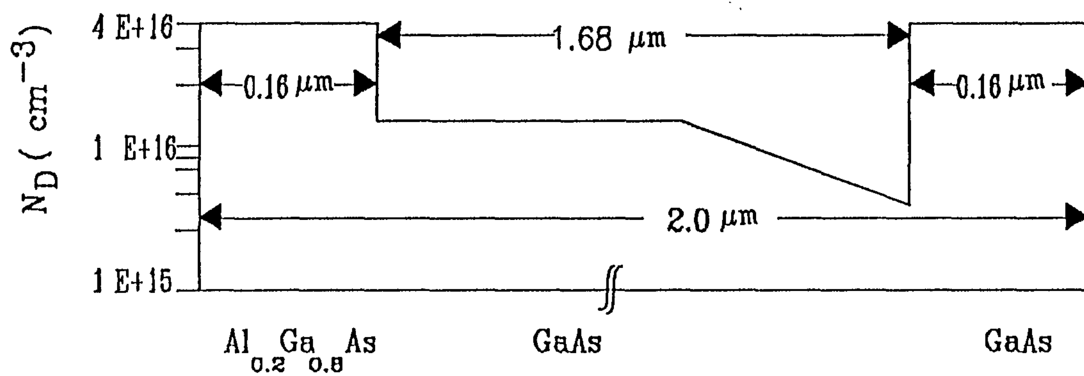

Figure 35. Simulated device structure for graded doping in the transit region.

carried out for a nonuniformly doped heterostructure, for the first time as shown in Figure 35. The device dimensions and the doping concentrations remained the same as shown in Figure 17 except for the fact that the last quarter portion of the transit region was doped in an exponentially decreasing manner. This reduced excess heating of electrons by the field near the anode and led to a higher efficiency as shown in Table III. Results are comprehensively discussed in the latter part of this chapter.

Finally, a comparative study between the conventional and heterostrucure devices is summarized in Table III. This table shows RF performance of the Gunn oscillators for four different configurations. 'Notch' in the table represents the results obtained for the conventional notch type oscillator for different biasing conditions. ' Hstrl and Hstr2 ' correspond to $Al_xGa_{1-x}As$ heterostructure oscillators with the composition x being equal 0.30 and 0.20 respectively. ' Hstr3 'represents the use of linearly graded $Al_xGa_{1-x}As$ injector. The value of the fractional alloy composition 'x' varied linearly from x=0 at the cathode to x=0.2 at the AlGaAs/GaAs interface. Finally ' Hstr4 ' denotes the heterostructure oscillator having nonuniform doping in the transit region in a logarithmic fashion. V_b is the dc bias voltage, f is the frequency of the signal current obtained from the simulations, P_s is the time-averaged power supplied by the battery to the circuit, P_d is the total power dissipated in the device (ac and dc), P_{ac} is the ac power delivered to the load resistor, η is the efficiency, defined as the ratio between the ac power delivered to the load and the time-averaged power supplied by the battery and x is the Al mole fraction.

Table III. RF Performance of Gunn Oscillators

Type	V_b (V)	f(GHz)	P_s (W)	P_d (W)	P_{ac} (W)	η (%)	x
Notch	2.0	66.67	2.136	1.962	0.0285	1.34	0.00
	2.5	67.57	2.616	2.306	0.0638	2.44	0.00
	3.0	68.12	3.000	2.665	0.0433	1.44	0.00
Hstr1	2.0	60.24	2.987	2.802	0.0297	0.99	0.30
	2.5	61.73	3.757	3.371	0.0562	1.40	0.30
	3.0	63.29	4.464	4.112	0.0799	1.78	0.30
Hstr2	2.0	62.55	2.994	2.795	0.0339	1.14	0.20
	3.0	64.15	4.047	3.621	0.0815	2.01	0.20
Hstr3	2.0	60.29	2.983	2.756	0.0338	1.14	0.20
	3.0	64.15	4.444	3.936	0.0777	1.75	0.20
Hstr4	2.0	63.35	3.064	2.888	0.0478	1.56	0.20
	3.0	66.72	4.478	3.916	0.0815	1.82	0.20

In agreement with the previous simulations [43], all the parameters listed in Table III increase with the dc bias voltage for notch oscillator. The underlying physical mechanism is an increase in the negative differential conductivity of the semiconductor at higher electric fields. Hstr1 oscillator, with the replacement of the GaAs cathode region with $Al_xGa_{1-x}As$, facilitates domain formation by carrier injection into theactive region at an energy which is very close to the band edge of the L valley. As can be seen from Table III, the ac power delivered by this configuration is significantly less than that for the conventional notch oscillator. Also, the efficiency is lower and the frequency of oscillation is significantly lower. This is probably due to the high energy injection from the ballistic launcher. Electrons acquire large kinetic energies, which increases carrier heat loss through phonon scattering. In the Hstr2 oscillator, with a lower Al mole fraction in the cathode, the electrons are injected into the active layer at a lower energy, and consequently Γ-L intervalley transfer does not occur as close to the heterointerface as in the previous example. We examined the results for an Al mole fraction of $x = 0.20$ in the cathode region. This configuration has a better microwave performance than the Hstr1 oscillator. The lower injection energies keep the power losses within the device to lower levels. For the Hstr3 oscillator, the simulations show that the point of accumulation layer formation is more insensitive to bias with the compositionally graded injector in place. Finally, implementation of ‘ Hstr4 ’ structure has led to a more optimized performance level than Hstr3 oscillator by generating larger voltage swings and more power with relatively higher efficiencies. The built-in electric fields provided by the intentional nonuniform doping within the active region work to suppress carrier heating.

Chapter 5

SUMMARY AND CONCLUSIONS

5.1 Concluding Summary

A model for the self-consistent Ensemble Monte Carlo simulation of both conventional and heterostructure Gunn oscillators has been developed. The effect of an external circuit has been incorporated into the calculations which facilitates a study of the circuit controlled phenomena. All the internal microscopic details of electronic transport which ultimately limit the high frequency response have been built in. The numerical scheme also includes all time dependent changes in the device boundary conditions self-consistently. Results for the notch configuration compare very well with previous studies. Calculations with heterostructures, at least at the fundamental mode, show some improvements in the efficiency and ac power output.

Theoretical results for the oscillating output voltages for the Gunn diode have been obtained for initial DC bias conditions of 2 and 3 Volts. A definite conclusion is that the heterostructure Gunn diode has shown improvement in performance against conventional Gunn devices. The Hstr1 and Hstr2 structures show a better AC-DC power ratio than the notch oscillator, as well as a better efficiency. We have demonstrated that the dead zone in a conventional Gunn device can be reduced by a suitable combination of a graded $Al_xGa_{1-x}As$ layer. The concept that electrons may be given an energy equivalent to the

intervalley separation by injecting them from a heterojunction has been verified. Further improvement in these devices was verified by incorporating a nonuniformity in the doping profile in a logarithmic manner in the transit region. By doing so, excess heating of electrons by the field near the cathode is reduced and higher efficiency was observed.

5.2 Suggestions for Future Work

Most of the work has been carried out using standard or near-standard microwave device structures composed of GaAs and AlGaAs materials. These heterostructures offer a variety of opportunities to design the cathode region which promise reduced transit times for high-frequency performance. Among the design options most frequently proposed are the compositionally graded cathode for hot electron injection, and the use of logarithmic variation of doping profile in the transit region. A Monte Carlo study of these design options has shown that each of these ideas has merit, but that the enhancements in the device performance realized by each approach are limited by the high rate of intervalley scattering in AlGaAs and GaAs. To take full advantage of these design ideas, a material with large Γ-L separation is desired. One such material is $In_xGa_{1-x}As$. The Γ-L separation is a 0.55 eV as compared to 0.3 eV for GaAs. This feature along with the small Γ-valley effective mass ($m_\Gamma^* = 0.0375m_o$) and the very large carrier mobility (13,770cm^2/V-sec) compared with the value of GaAs (8500 cm^2/V-sec) makes $In_xGa_{1-x}As$ an extremely attractive cathode material for high performance devices. One other material is InP whose cutoff frequency for the transferred electron effect has been predicted to be approximately a factor of two higher than GaAs [44]. So it becomes

evident that GaAs may be improved by using InP or other Indium based alloys. However, alloying introduces an additional scattering mechanism into the problem which has to be taken into account when assessing the virtues of ternary and quarternary materials.

The possible development of these devices are mainly governed by the power and efficiency at a given frequency. The various causes of power and efficiency limitations are (i) thermal dissipation, (ii) space-charge effects, and (iii) impedance requirements. Thermal dissipation can be reduced by using annular or cross device structure by about 20 or 25% [45]. To avoid space-charge effects, the carrier concentration should not deviate very much from the doping level in order to prevent impact ionization and build up of strong nonuniform electric fields in the transit region. This, in the present case, has effectively been achieved by tailoring the doping profile. The third cause of power limitation is the minimum matchable impedance in microwave circuits. This occurs, because it is not possible to design a microwave circuit whose resistance is much smaller in magnitude negative resistance of the device.

Having considered the ways to overcome the above limitations, we proceed to discuss the other improvements that need to be included in the modelling. The current simulations have been performed with a sample circuit structure operating in the fundamental mode of oscillation. For practical applications, at the frequency range we explore, it is more common to use circuits operating in the harmonic mode, which are easier to fabricate and tune. Our model could be extended to the harmonic operation with straight forward modifications [46], by loading the Gunn diode with a number of parallel resonant circuits connected in series and tuned to the harmonic frequencies.

Another ingredient that would prove crucial in our design is the incorporation of a very thin n^+ GaAs layer sandwiched between the graded gap and the transit region [47]. This layer may be thought of as a very short wire: it could allow the hot electron properties to be retained while still permitting us to use its depletion effects to control the size of the electric field at the start of the drift region.

The next stage in the advancement of Gunn diode design could be to use the combination of the hot electron injection at the cathode and the variation of the doping profile in the transit region in a logarithmic manner from high at the cathode to low at the anode. This technique will produce diodes where the electric fields will have been engineered throughout the whole device with, it is hoped, yet further improvements in device performance.

Finally, using the current simulation scheme, one could work to extract the frequency dependent transfer function for Gunn diodes. Effective parameter extraction and simulation of the impedance values constitute important extensions for circuit applications.

References

[1] S. D. Hersee, B. Cremoux de, and J. P. Duchemin, "Some Characteristics of GaAs/AlGaAs Graded Index Separate Confinement Heterostructure Quantum Well Laser Structure," Applied Physics Lett., **44**, p. 476, 1984.

[2] R. Fisher, and H. Morkoc, "Modeling of GaAs/AlGaAs Devices-A Critical Review," IEEE Circuits and Devices Magazine 1, p. 35, 1985.

[3] M. P.Shaw, Solomon, P.R. and H. Grubin, "The Gunn-Hilsum Effect," Academic Press, New York, 1979.

[4] For example, see the IEEE Trans. Electron Devices, 13, Jan. 1966 special issue.

[5] J. R. Hauser, T. H. Glisson, and M. A. Littlejohn, "Negative Resistance in III-V Semiconductors," Solid State Electr., **22**, p. 487, 1979.

[6] C. Patel, T. J. Parker, H. Jamshidi, and W. F. Sherman, Phys. Stat. Sol. B **122**, p 461, 1984.

[7] J. Shah, B. Deveaud, T.C. Damen, W. T. Tsang, A. C. Gossard, and P. Lugli, "Determination of Intervalley Scattering Rates in GaAs by Subpicosecond Luminescence Spectroscopy," Phys. Rev. Lett. **59**, p. 2222, 1987.

[8] For example, N. R. Couch, P. H. Beton, T. M. Kerr, D. J. Knight, and J. Ondria, "The Use of Linearly Graded Composition AlGaAs Injectors for Intervalley Transfer in GaAs: Theory and Experiment," Solid State Elec. **31**, p. 613, 1988.

[9] J. A. Copeland, "LSA Oscillator Diode Theory," J. Appl. Phys. **38**, p. 3096, 1967.

[10] D. Jones and H. D. Rees, "Accumulation Transit Mode in Transferred Electron Oscillators," Electron. Lett. **8**, p. 566, 1972.

[11] R. Bosch and H. W. Thim, "Computer Simulation of Transferred Electron Devices using the Maxwellian approach," IEEE Trans. Elec. Dev., **21**, p. 16, 1974.

[12] P. A. Lebwohl and P. Price, "Direct Microscopic Simulation of Gunn-Domain Phenomena," Appl. Phys. Lett. **19**, p. 530, 1971.

[13] D. E. Aspnes, C.G. Olson, and D. W. Lynch, "Ordering and Absolute Energies of the L_c^6 and X_c^6 Conduction Band Minima in GaAs," Phys. Rev. Lett. **37**, p. 766, 1976.

[14] J. W. Tully, "Monte Carlo Simulation of Millimeterwave Gunn Effect Relaxation Oscillator," IEEE Trans. Elec. Dev. **ED-34**, 1983.

36 [15] M. M. Atalla and J. L. Moll, "Emitter Controlled Negative resistance in GaAs," Solid State Electron., **12**, p. 619, 1969.

[16] Herbert. K, "Hot Electron Relaxation Effects in Devices," IEEE Trans. Elec. Dev., p. 61, 1978.

[17] Paul F. Combes, "Microwave Components, Devices, and Active Circuits," p. 131, 1987.

[18] H. Kroemer, "Theory of the Gunn Effect," Proc. IEEE, **52**, p. 1736, 1964.

[19] B. K. Ridley, "Specific Negative Resistance in Solids," Proc. Phys. Soc. Lond., **82**, p. 954, 1963.

[20] H. Kroemer, "Negative Conductance in Semiconductors," IEEE Spectrum, **5**, p. 47, 1968.

37 [21] J. A. Copeland, "A New Mode of Operation for Bulk Negative Resistance Oscillators," Proc. IEEE, **54**, p. 1479, 1966.

[22] G. S. Hobson, The Gunn Effect, Clarendon, Oxford, 1974.

38 [23] B. K. Ridley, "Anatomy of the Transferred-Electron Effect in III-V Semiconductors, "J. Appl. Phys., **48**, p. 754, 1977.

39 [24] Ondria, J. and Ross, R. L., 17th European Microwave Conference Digest, p. 673, Sept. 1987.

[25] E. M. Conwell, "High Field Transport in Semiconductors," Solid State Phys., Suppl. 9, 1967.

[26] H. Budd, "Hot Carriers and the Path Variable method," J. Phys. Soc. Japan, **21**, p. 420, 1966.

[27] T. Kurosawa, J. Phys. Soc. Jpn. Suppl. A 49, p. 345, 1966.

[28] S. N. Chamoun, R. Joshi, E. N. Arnold, and R. O. Grondin, " Theoretical and Experimental Investigations on Subpicosecond Photoconductivity," J. Appl. Phys., **66**, p. 236, 1989.

[29] H. D. Rees, J. of Phys. Chem. Solids, **30**, p. 643, 1969.

[30] W. Fawcett, A. D. Boardman, and S. Swain, "Monte Carlo Determination of Electron Transport Properties in GaAs," J. Phys. Chem. Solids, **31**, p. 1963, 1970.

[31] J. B. Gunn, "Instabilities of Current and of Potential Distribution in GaAs and InP," in Plasma Effects in Solids. New York: Academic, p. 199, 1965.

[32] J. A. Copeland, "Electrostatic Domains in Two-Valley Semiconductors," Trans. IEEE on Electron Devices, **13**, p. 189, 1966.

[33] H. W. Thim, "Computer Study of Bulk GaAs Devices with Random One-Dimensional Doping Fluctuations," J. Appl. Phys., **39**, no. 8, p. 3897, 1968.

[34] P. A. Blakey and R. K. Froelich, "On the Transient Analysis of Circuits containing multiple Diodes," IEEE Trans. Microwave Theory Tech., MTT-31, p. 781, 1983.

[35] H. Spooner and N. R. Couch, "Advances in Hot Electron Injector Gunn Diodes," GEC Journal of Research, **7**, P. 35, 1989.

[36] M. Heilblum, M. I. Nathan, D. C. Thomas, and C. M. Knoedler, "Direct Observation of Ballistic Transport in GaAs," Phys. Rev. Lett., **55**, p. 2200

[37] J. R. Hayes, A. F. J. Levi, and W. Weigmann, "Hot Electron Spectroscopy of GaAs," Phys. Rev. Lett., **54**, p. 1570, 1985.

[38] A. P. Long, P. H. Beton, and M. J. Kelly, "Hot Electron Transport in heavily doped GaAs,", Semiconductor Sci. Tech., 1, p. 63, 1986.

[39] A. P. Long, P. H. Beton, M. J. Kelly, and T. M. Kerr, "Hot Electron Injection by Graded AlGaAs," Electron Lett., **22**, p. 1321, 1986.

[40] I. Hase, H. Kawai, S. Imanga, K. Kaneko, and N. Watanabe, "AlGaAs/GaAs hot electron transistor grown by MOCVD," Inst. Phys. Conf. Series, **79**, p. 613, 1985.

[41] J. M. Shannon, "A majority carrier camel diode," Appl. Phys. Lett. **35**, p. 63, 1979.

[42] Beall, R. B., Harris, J. J, Szubert, J. M., and Barstow, J., Philips Annual Report, 32, 1987.

[43] Christopher H. Lee and Umberto Ravaioli, "Performance Evaluation of Heterojunction Cathode Gunn Oscillators using Monte Carlo Simulations," to appear in IEEE Trans. Elec. Dev., 1991.

[44] Crowley, J. D., Sowers, J. J., Janis, B. A., and Fank, F. B., "High Efficiency 90 GHz InP Gunn Oscillators," Electron. Lett., **18**, p. 705, 1980.

[45] Salmer, G., "Physical Frequency Limitations of 2-terminal Devices," Proc. of IEEE, **130**, p. 80, 1983.

[46] M. Curow and A. Hintz, "Numerical Simulation of Nonstationary Electron Transport in Gunn Devices in a Harmonic Mode Oscilltor Circuit," IEEE Trans. Electron Devices, **34**, p. 1983, 1987.

[47] P. H. Beton, A. P. Long, N. R. Couch, M. J. Kelly, "Use of n^+ Spike Doping Regions as Non-equilibrium Connectors," Electron. Lett., **24**, p. 434, 1988.